Construction of a Gas System for the CBM-TRD Prototypes and Analysis of CBM-TRD Test Beam Data Towards Position Reconstruction

Masterarbeit im Studiengang Physik

Felix Fidorra

Erster Gutachter: Prof. Dr. Christian Klein-Bösing
Zweiter Gutachter: Prof. Dr. Anton Andronic

13.08.2020

Westfälische Wilhelms-Universität Münster

Contents

1 Introduction

A large domain in the modern physics research is the investigation of the strong interaction. To examine interactions with a range of the scale of nuclei, large accelerators and large detector assembles are needed. In the near future one of these experiments will be the CBM (*Compressed Baryonic Matter*) experiment at FAIR (*Facility for Antiproton and Ion Research*). The Institut für Kernphysik Münster is one of the institutes involved in the development of the CBM-TRD (*Transition Radiation Detector*). Part of the development process is the testing of the TRD prototypes e.g. during testbeam campaigns at nuclear research facilities. One of those testbeam campaigns is the mCBM testbeam campaign which takes place at the accelerator facility SIS18 (*SchwerIonen Synchrotron*) at FAIR. A gas system to supply the TRD prototypes with a Xenon/Carbon Dioxide gas mixture has been build and will be presented in this work.
While in direct measurements not all parameters can be chosen freely, corresponding simulations can serve as proper tool for larger exploitation of the parameter space. The signals of the detectors were conducted to a shaper which displays the incoming charge in the parameter of the exported curve. The time evolution of the shaping time has been simulated to estimate the effects of the phasing on the charge distribution in time. A determination of the phase shift may give the possibility of a higher time resolution.
In addition, a simulation of the charge distribution on the pad plane has been done to test and improve the implemented position reconstruction algorithms.
The data of the DESY 2017 testbeam campaign has been analyzed under the aspects of the reconstruction efficiency and position reconstruction. First steps of a possible tracking algorithm are sketched.

2 Theory

2.1 Particles Interacting with Matter

To detect a particle in a detector, some kind of interaction with the detector material has to occur. In the following, the relevant interactions of particles with detector material will be discussed.

2.1.1 Heavy Charged Particles Interacting with Matter

The stopping power of charged particles heavier than electrons depends on the traversed material and on the projectile. For particles with a relativistic γ-factor between 0.1 and 1000, which the detected particles are expected to have, the Bethe equation describes the energy loss per distance:

$$\left\langle -\frac{\mathrm{dE}}{\mathrm{dx}} \right\rangle = K z^2 \frac{Z}{A} \frac{1}{\beta^2} \left[\frac{1}{2} \ln \frac{2 m_e c^2 \beta^2 \gamma^2 W_{max}}{I^2} - \beta^2 - \frac{\delta(\beta\gamma)}{2} \right]. \tag{2.1}$$

The constants and variables are named in Table 2.1 [T^+18]. At higher energies, additional Bremsstrahlung is produced, at lower energies the Anderson-Ziegler region takes place. The energy loss for a muon through a copper target is shown in Figure 2.1. The general shape of the graph is preserved but shifted for different absorber materials or projectiles. A matter of particular interest is the MIP (*minimal ionizing particle*) region. MIPs have the lowest energy deposition in the material and therefor shall be considered on choice of trigger threshold.

Table 2.1: The variables which are used in Formula 2.1 taken from [T^+18]

Symbol	Definition	Value or (usual) units
K	$4\pi N_A r_e^2 m_e c^2$ coefficient for dE/dx	$0.307075\,\mathrm{MeV mol^{-1} cm^2}$
z	charge number of incident particle	
Z	atomic number of target	
A	atomic mass of target	$\mathrm{g mol^{-1}}$
$m_e c^2$	electron mass times c	$0.510998941(31)\,\mathrm{MeV}$
W_{max}	maximum energy transfer possible in a collision	MeV
I	mean excitation energy	eV
$\delta(\beta\gamma)$	density effect correction to ionization energy loss	
N_A	Avogadro's number	$6.022140857(74) \cdot 10^{23}\,\mathrm{mol^{-1}}$

2.1.2 Electrons Interacting with Matter

The interaction process of electrons with matter differs significantly from the interaction of heavy particles with matter. The different kinematics, spin, charge, and the permutability with the shell

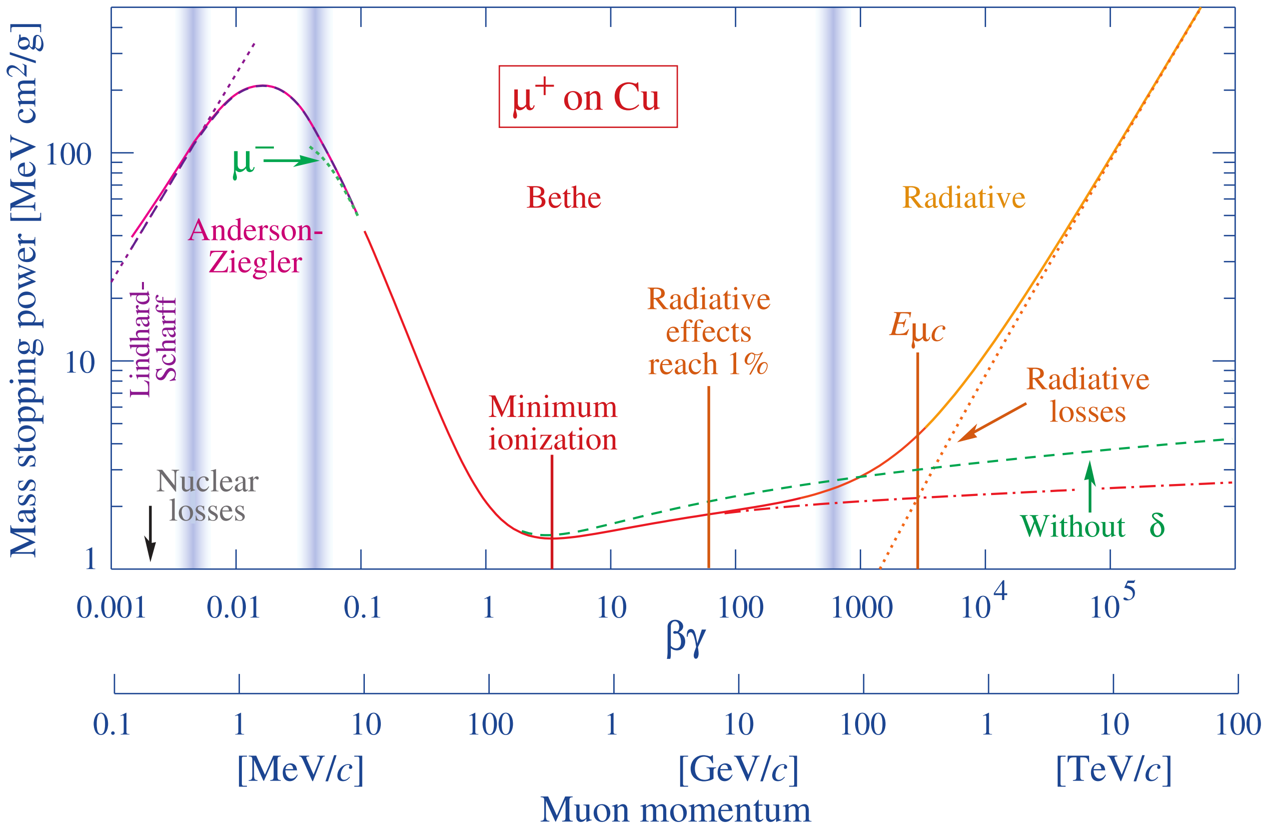

Figure 2.1: The energy loss of a muon hitting a copper target is shown. The *Bethe-equation* is applicable in the mid energy range. The minimum ionizing region is marked. [T+18]

electrons has to be taken into account.
At low energies, the interaction can be described with Møller scattering [T+18]:

$$\left\langle -\frac{dE}{dx} \right\rangle = \frac{1}{2} K \frac{Z}{A} \frac{1}{\beta^2} \left[\ln \frac{m_e c^2 \beta^2 \gamma^2 \{m_e c^2 (\gamma - 1)/2\}}{I^2} + (1 - \beta^2) - \frac{2\gamma - 1}{\gamma^2} \ln 2 + \frac{1}{8} \left(\frac{\gamma - 1}{\gamma} \right)^2 - \delta \right]. \tag{2.2}$$

The variables are used as described in Table 2.1.
At higher energies, Bremsstrahlung becomes the dominant energy loss effect. The radiation losses can be described with [Kle05]:

$$-\left(\frac{dE}{dx} \right)_{\text{brems}} = 4\alpha N_A \frac{Z^2}{A} r_e^2 E \ln \frac{183}{Z^{1/3}} = \frac{E}{X_0}. \tag{2.3}$$

The variables are defined as indicated in Table 2.1 with $\alpha = e^2/(4\pi\epsilon\hbar c) \approx 1/137$, the fine structure constant [Kle05]. X_0 is the radiation length. It is defined as the layer thickness at which an electron loses all but $1/e$ of its energy. Also, it describes the length a photon travels until its electron-positron production probability reaches $P = 1 - \exp(-7/9) \approx 54\%$. The radiation length is given by the formula [Kle05]:

$$\frac{1}{X_0} = r_e^2 4\alpha Z^2 \frac{N_A}{A} \ln \frac{183}{Z^{1/3}}. \tag{2.4}$$

For very high energies, the energy loss can be calculated with

$$-\frac{dE}{E} = \frac{dx}{X_0}. \tag{2.5}$$

The energy loss in dependence of the particle energy is shown in Figure 2.2.

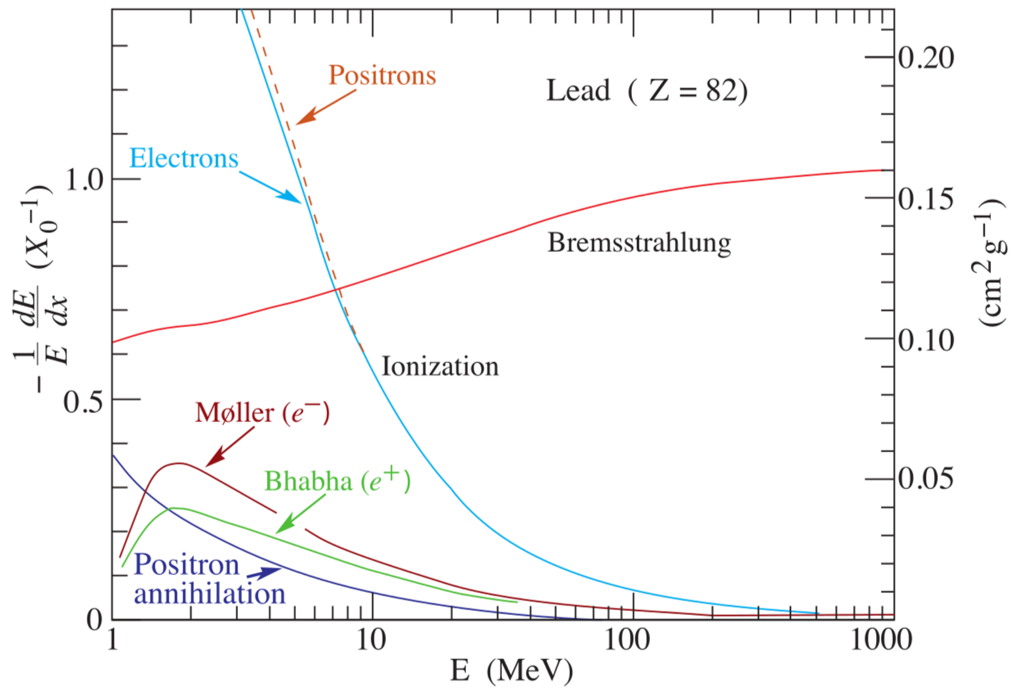

Figure 2.2: The energy loss of electrons and positrons in Lead is shown. At low energies, Møller scattering takes place. At higher energies, bremsstrahlung becomes the dominant effect. [T+18]

2.1.3 Photons Interacting with Matter

If a photon hits a target, three different interactions may appear. At the low energy region ($E_\gamma \leq 100\,\mathrm{keV}$), the photoelectric effect is the primary interaction effect. At the medium energy domain ($E_\gamma \approx 1\,\mathrm{MeV}$), the compton effect becomes dominant and at high energies, ($E_\gamma \approx 2\,\mathrm{GeV}$), the pair production has the highest cross section [Kle05].

Photoelectric Effect

When a low energy photon interacts with an atom, the photon gets absorbed and transfers the whole energy to a shell electron which is then no longer bound in the atom. The energy threshold for this effect the binding energy of the electron. The binding energy is a property of the target material and each element has its own characteristic absorption lines.

Compton Scattering

When Compton scattering occurs, the photon does not transfer the whole energy to the electron. The ratio of the transferable energy which is transmitted depends on the scattering angle. Taking momentum conservation into account, the energy of the photon can be written as:

$$E'_\gamma = \frac{E_\gamma}{1 + (E_\gamma/m_e c^2)(1 - \cos\theta)}. \tag{2.6}$$

In this equation E_γ and E'_γ are the photon energies before and after the scattering process and θ is the scattering angle [Kle05].

Electron-Positron Pair Production

For high energy photons ($E_\gamma \geq 1.022\,\mathrm{MeV} = 2m_e$), an electron-positron pair can be produced. The excess momentum is transferred to the target with a virtual photon[Kle05][T$^+$18].

Each of these interactions removes the photon from a directed beam. The intensity loss in the interacting material can be calculated by:

$$I(x) = I_0 e^{-\mu x}. \tag{2.7}$$

μ is called the mass absorption coefficient.

The TR-photons produced by the CBM-TRD radiator have an energy roughly between 5 keV and 20 keV [tdr18]. Thus, the photoelectric effect is the only interaction mechanism which will occur.

2.2 Production of Transition Radiation

If a particle passes the border between two media with a difference in the dielectric constants ϵ_1, ϵ_2, TR (*Transistion Radiation*) may be produced. The double differential energy spectrum is given by [AW12]:

$$\frac{d^2W}{d\omega d\Omega} = \frac{\alpha}{\pi^2}\left(\frac{\Theta}{\gamma^{-2} + \Theta^2 + \zeta_1^2}\frac{\Theta}{\gamma^{-2} + \Theta^2 + \zeta^2}\right)^2 \tag{2.8}$$

with $\gamma \gg 1$, $\zeta_1^2, \zeta_2^2 \ll 1$, $\Theta \ll 1$, $\Theta_i^2 = \omega_{P_i}^2/\omega^2 = 1 - \epsilon_i(\omega)$, where ω_{P_i} is the electron plasma frequency:

$$\omega_P = \sqrt{\frac{4\pi\alpha n_e}{m_e}} \approx 28.8\sqrt{\rho\frac{Z}{A}}\ \mathrm{eV} \tag{2.9}$$

where n_e is the electron density of the medium [AW12], [T$^+$18]. Due to the fact that the emission angle Θ is small an integration leads to a differential energy spectrum per interface [AW12]:

$$\left(\frac{dW}{d\omega}\right)_{interface} = \frac{\alpha}{\pi}\left(\frac{\zeta_1^2 + \zeta_2^2 + 2\gamma^{-2}}{\zeta_1^2 - \zeta_2^2}\ln\frac{\gamma^{-2} + \zeta_1^2}{\gamma^{-2} + \zeta_2^2} - 2\right). \tag{2.10}$$

The TR spectrum for a single interface transition and a transition for one foil (two interfaces) is shown in Figure 2.4, irregular radiators require a more complex description.

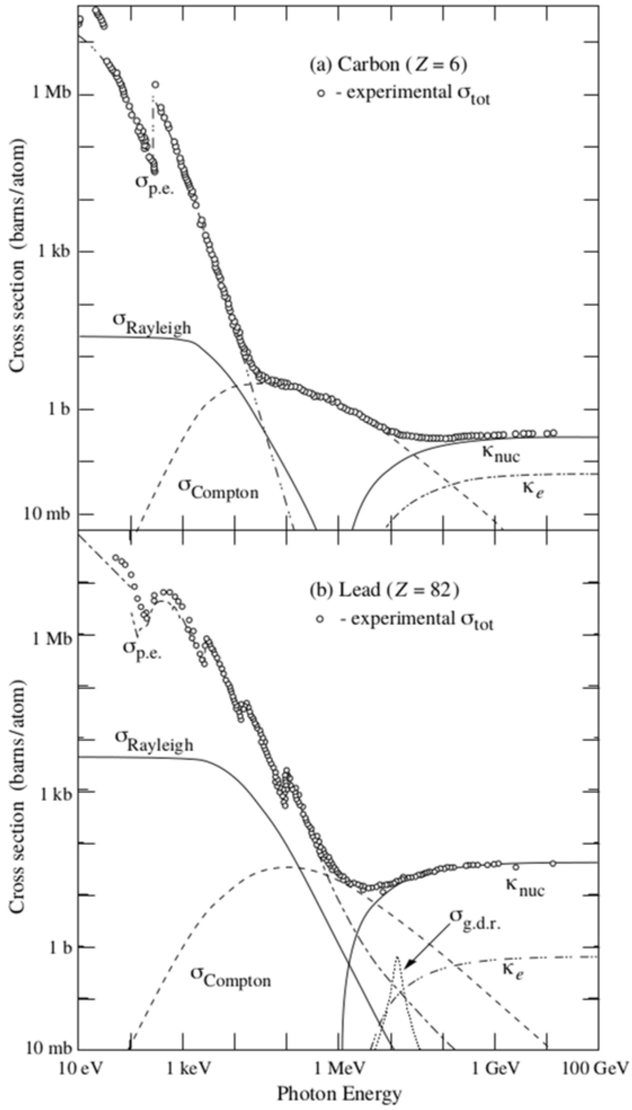

Figure 2.3: The interaction cross section for photons passing through Lead and Carbon is shown. In the low energy region, the ionization mechanism is dominant. The steps in the cross section are caused by the absorption lines of the atoms. Compton scattering sets in at a few eV and becomes dominant at a few 100 keV. Pair production starts at 1.022 MeV and becomes the leading effect at a few 100 MeV. The precise numbers depends on the used absorption material [T^+18].

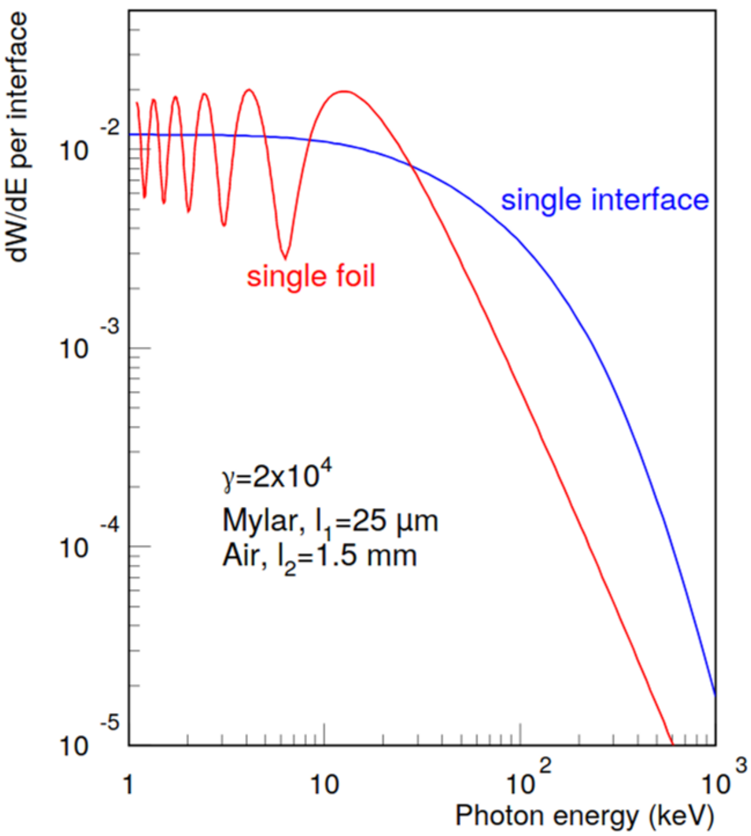

Figure 2.4: TR spectrum for single interface and single foil configurations is shown. [AW12]

3 Transition Radiation Detector for the CBM Experiment

This chapter describes the CBM-TRD in a general manner. The detector has to fulfill the requirements on physics reconstruction. An electron efficiency of 90 % with a pion suppression factor about 20 is needed. The signal collection time has to stay below 300 ns and the hit rate per channel below 100 kHz. To enable efficient track matching, the position resolution has to be less than 300 μm [tdr18].

3.1 Multi Wire Proportional Chamber

3.1.1 General Case

The basic principle of an MWPC (*Multi Wire Proportional Chamber*) is similar to the working principle of a proportional counter.
A typical chamber consists of two cathode planes which limit the gas volume. Between those cathode planes, a wire plane is installed. In the symmetrical case, the distance between the wires and the planes is equal in both directions. See Figure 3.1.

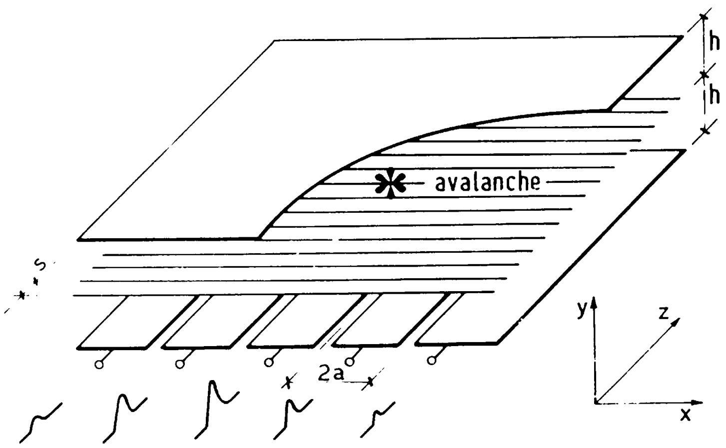

Figure 3.1: A scheme of a symmetrical MWPC is shown. The distance h between the wires and the cathode planes is equal. [BRR08]

A voltage is applied between the cathode planes and the anode wires. When a charged particle passes the detector, it ionizes the gas along its trajectory. The electrical field separates the electrons from the ions, the ions drift in the direction of the cathode planes and the electrons drift to the anode wires. Nearby the anode wires the electric field gradient increases strongly leading to an increase of the electrons kinetic energy. In this region the electrons have enough energy to ionize additional gas atoms and an electron cascade is created, as shown in Figure 3.2. This electron cloud induces a signal at the cathode plane. The direct signal is measurable at the wires and the induced signal is measurable at the cathode plane.

Figure 3.2: A scheme of the cross section of an anode wire is shown. The black dots represent the electrons, the circle represents the wire cross section. Nearby the wire, an electron avalanche is created and produces the signal. [BRR08]

3.1.2 CBM-TRD MWPC

In the case of the CBM-TRD, a non symmetrical chamber is used, see figure 3.3. At the front side of the detector, the gas volume is extended and an additional cathode wire layer is integrated. To get a symmetric amplification region, the distance between the cathode wire layer and the anode wire layer and the distance between the back plane and the anode wires are identical. Electrons which are created in the drift region drift along the electric field lines towards the anode wires. The drift region has a thickness of 5 mm and the two amplification regions have a thickness of 3.5 mm each.

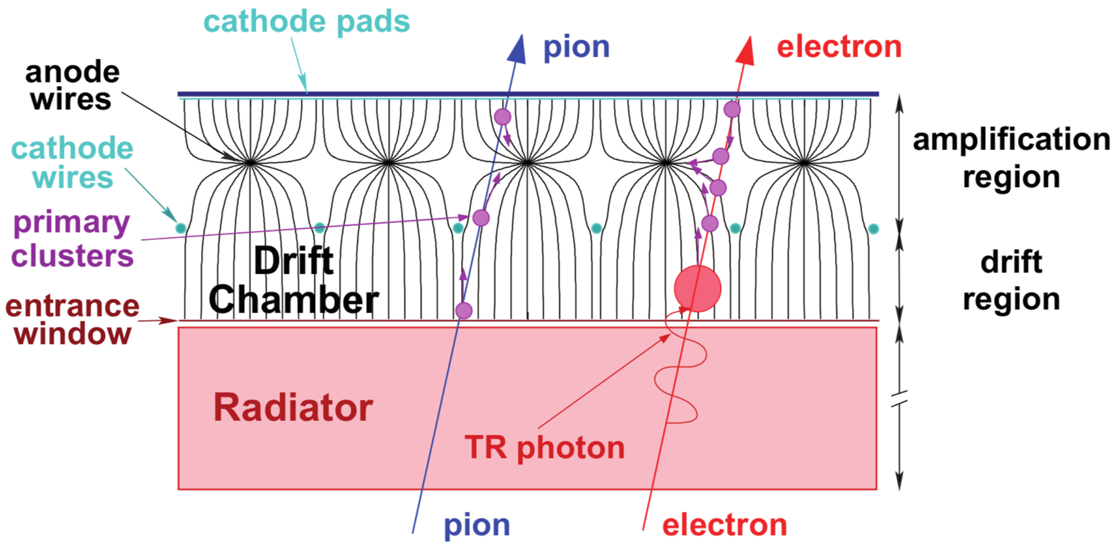

Figure 3.3: In this scheme, the black lines represent the electric field lines. The chamber is separated in two regions. In the drift region, the created charge is divided in a way such that electrons and ions move along the electric field lines. In the amplification region, close to the wires, the electron avalanche and the amplification process take place. [tdr18]

The back panel consists of the pad plane which is glued on a mechanical support structure. This stabilization is made of a honeycomb structure, a carbon plane, and an Aluminum frame. The back panel has four holes for the gas inlet. The anode wires are made of Gold plated Wolfram. They have a diameter of 20 μm and a distance to each other of 2.5 mm. The cathode wires are made of a Copper Beryllium alloy. They have a diameter of 75 μm, and also a distance of 2.5 mm between each other. The anode wire grid is shifted by 1.25 mm compared to the cathode wire grid. The back plane of the detector has a substructure of small rectangular pads. The dimensions of those rectangular pads depend on the chamber model which is used. The pads in the detector which was used at the DESY 2017 testbeam have a length of 15.67 cm, a width of 0.73 cm, resulting in an area of 11.50 cm^2. To calculate these physical dimensions, the whole active area, 940 mm $\times$ 940 mm, was divided by the number of rows and columns. To make sure that none of the pad borders is below an anode wire, the length of the pads are slightly varied in accordance with the before mentioned regular division. The pad plane geometry was designed by D. Emschermann, see Figure 3.4.

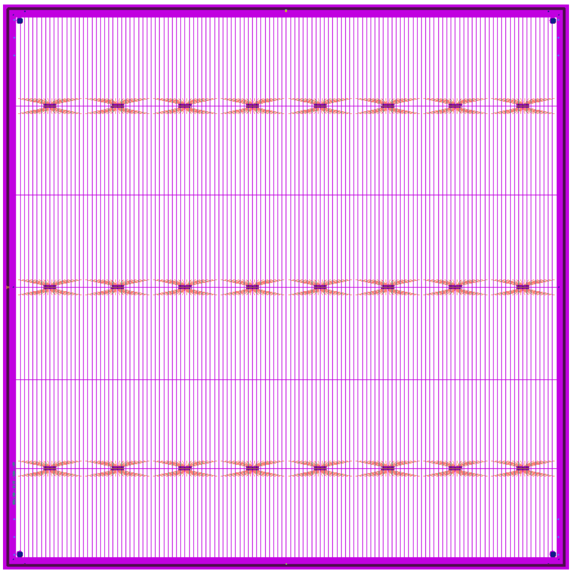

Figure 3.4: The pad plane design is of the type 8. This layout has six rows and 128 columns. The pad plane was designed by D. Emschermann [pad20].

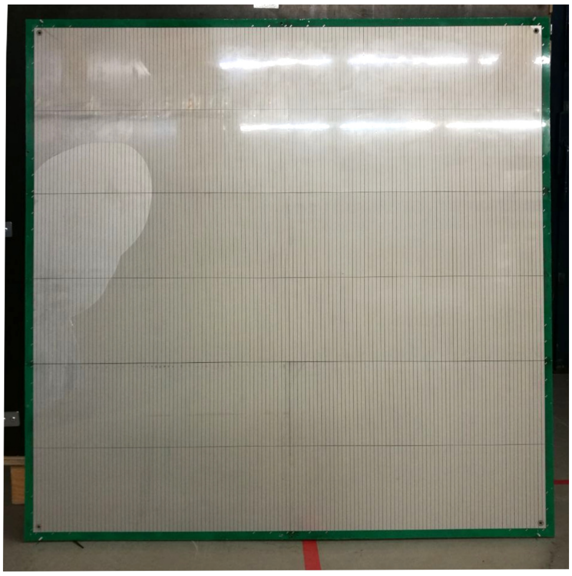

Figure 3.5: A back plane of the type which was used in the 2017 prototypes. Each plane of this type has six rows and 128 columns. This design was developed in 2015.

The front side and entrance window of the detector is made of an aluminum plated Kapton foil. The entrance window is strengthened with a carbon support grid to hold it in shape. All layers of the detector are shown in Figure 3.6.

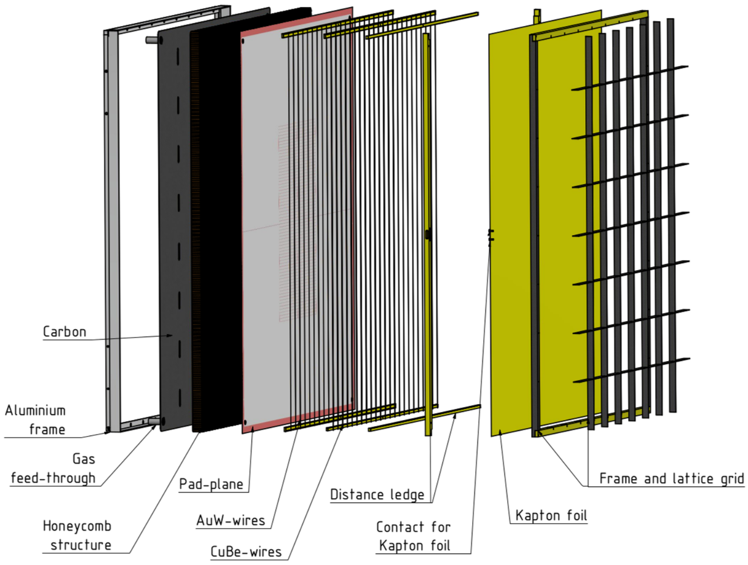

Figure 3.6: A stretched, photo realistic CAD (*Computer aided Design*) sketch of the readout chamber is shown. [tdr18]

3.2 Pad Response Function

To achieve a high position resolution, the charge distribution on the pad plane has to be known. An empirical formula, the PRF (*Pad-Response-Function*) of this type of pad plane, has been found by E. Mathieson et al [Mat88]:

$$PRF(d/h) = \int_{d/h-W/2}^{d/h+W/2} \rho(d'/h)\mathrm{d}(d'h/h) = -\frac{\arctan\left(\sqrt{K_3}\tanh\left(\pi\left(\sqrt{K_3}-2\right)\cdot\frac{W-2\cdot d}{8h}\right)\right)}{2\arctan\left(\sqrt{K_3}\right)} - \frac{\arctan\left(\sqrt{K_3}\tanh\left(\pi\left(\sqrt{K_3}-2\right)\cdot\frac{W+2\cdot d}{8h}\right)\right)}{2\arctan\left(\sqrt{K_3}\right)}. \tag{3.1}$$

K_3 is a parameter which depends on the wire geometry and has been determined to be 0.38 [Ber14]; $W = 0.73\,\mathrm{cm}$ is the pad width; $h = 15.67\,\mathrm{cm}$ is the distance between the anode wire and the pad plane; d is the displacement. The displacement is the distance between the pad center of the central pad and the center of the charge distribution.

The charge distribution is shown in Figure 3.7.

To calculate the displacement, different methods can be used. In the following, methods to reconstruct a three pad cluster will be presented. Each pad has a charge information Q_i and a position information, the displacement to the center, d_i. The central pad has the index i.

Center of Gravity (COG), the center of gravity algorithm is described in formula 3.2

$$d_{cog} = \frac{Q_{i-1}d_{i-1} + Q_i d_i + Q_{i+1}d_{i+1}}{Q_{i-1} + Q_i + Q_{i+1}}. \tag{3.2}$$

This algorithm is expandable and able to reconstruct the position of a four pad or even bigger cluster. It is strongly biased towards the pad center. This will be discussed in section 5.2.

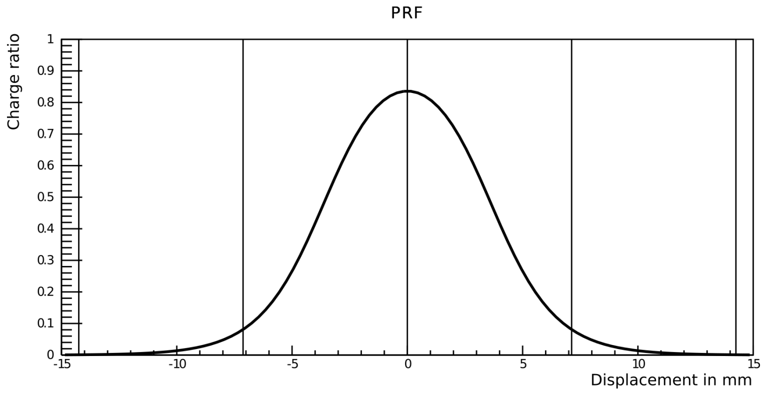

Figure 3.7: The charge ratio of a pad in dependence of the displacement is shown. The vertical lines represent exemplary the pad centers. [Mun16]

Hyperbolic secant squared method (SECH) is described by:

$$d_{sech} = \frac{a_3}{\pi} \text{arctanh} \left(\frac{\sqrt{Q_i/Q_{i-1}} - \sqrt{Q_i/Q_{i+1}}}{2\text{sinh}((\pi W)/a_3)} \right) \tag{3.3}$$

with

$$a_3 = \frac{\pi W}{\text{arccosh}\left(0.5 \cdot \left(\sqrt{Q_i/Q_{i-1}} + \sqrt{Q_i/Q_{i+1}}\right)\right)}.$$

This algorithm is applicable only for a three pad cluster but is less biased towards the pad center than the COG algorithm.

3.2.1 Position Reconstruction

To get a high position resolution, the back plane of the detector is separated in small rectangular pads. The described algorithms only allow a high position resolution along the wire direction, this is parallel to the short borders of the pads. To get a high position resolution in both direction, each second layer is rotated by 90 °.

3.3 Radiator

The radiator which was used at the DESY 2017 testbeam is made of polethylene (PE) foam foils. Each of the foils has a thickness of roughly 2 mm and 146 foils were put together in a box made of Rohacell HF71. The outer dimensions of the radiator are 99 cmx99 cm with a thickness of 30 cm, see Figure 3.9. Due to the carbon grid on the Kapton foil, small gaps remain between the entrance window and the radiator. These gaps are filled with seven pieces each of the radiator foam foil to avoid the absorption of TR photons, but also still contributing to the generation, see Figure 3.8.

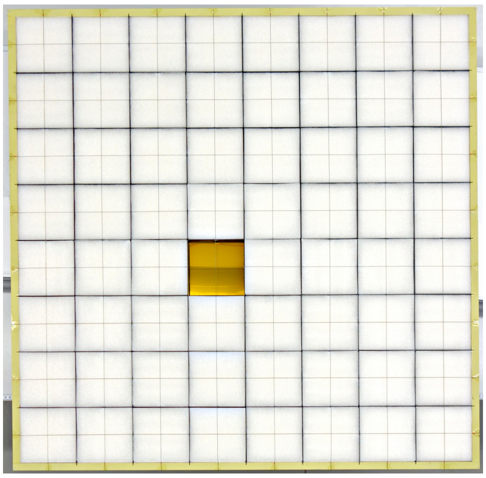

Figure 3.8: The front side of the detector is shown. The gaps between the entrance window and the radiator are also filled with small PE foam foils. One of the gaps is not filled to perform measurements without the radiator. [tdr18]

Figure 3.9: A radiator which was used at the DESY 2017 Testbeam is shown. The outer dimensions are 99 cm x 99 cm x 30 cm.[tdr18]

3.4 Readout Electronics

3.4.1 SPADIC

The main part of the CBM-TRD readout chain is the SPADIC (*Self-triggered Pulse Amplification and Digitization asIC*) with 32 input channels, mounted on the FEB (*Front-End-Board*). In this thesis, SPADICs of the revision 2.0 were used, which main specifications are reported in the following. The SPADIC consists of two main parts. The digital backend which communicates with the AFCK and the readout part with the analog-digital converter, see Figure 3.10.
The CSA (*Charge Sensitive Amplifier*) has an adjustable amplifier and shaper which, upon charge injection creates a signal with the shape:

$$f(t) = A \cdot \frac{t}{\tau} \cdot \exp\left(-\frac{t}{\tau}\right) \quad (\text{for} \quad t \geq 0)\,. \tag{3.4}$$

The SPADIC 2.0 has a peaking time of $\tau = 240\,\text{ns}$ [tdr18]. The free parameter t is according to the inserted charge, A is the amplification factor.
The ADC (*Analog Digital Converter*) is a custom pipeline converter. The digitized signal is separated in 32 time bins. Each sample has a length of 62.5 ns, thus the whole signal has a length of 2 ms.
The DSP (*Digital Signal Processor*)element is a mask which selects predefined parts of the inserted pulse that are sufficient to characterize the whole shape. Due to the fact that the analysis of the behavior of the chamber and of the SPADIC is not finished, yet, the DSP element passes the whole pulse through. This enables a more detailed view of the signal.
The Hit Logic is the part of the chip where the trigger and the classification of the hits take place.

Hit Logic

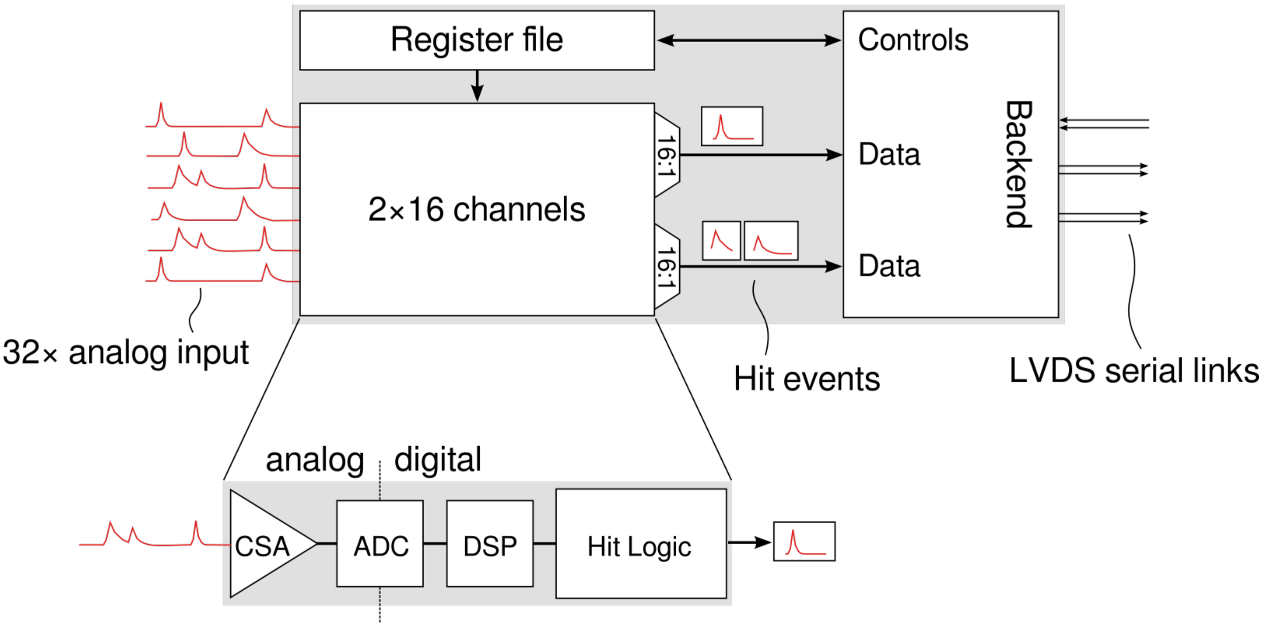

Figure 3.10: Schematic drawing of the SPADIC. The readout electronic consists of 2 times 16 channels. Each channel has a CSA (*Charge Sensitive Amplifier*), an ADC (*Analog-to-Digital Converter*), a DSP (*Digital Signal Processor*), and a Hit Logic. In the utilized version of the SPADIC, the backend communicates via E-link. [tdr18]

To pass the trigger threshold, a hit has to fulfill the condition:

$$t = [(a \leq t_1) \wedge (b \leq t_2)] \vee (b > t_1) \vee (c > t_2). \tag{3.5}$$

t_1 and t_2 are two selectable thresholds and a, b, and c are the ADC values of three successive samples [Fis]. If a channel is triggered, the values of the time bins are recorded. The signal is sampled in 32 time bins. Two of them are presamples, i.e., samples before the real trigger signal, and are stored in the shift register of the SPADIC. The taken signal is called *self triggered*. A self triggered channel passes a trigger signal to its neighbors. Two channels are called neighbors if their corresponding pads on the pad plane are physically neighbored. The consequently triggered channels are called *neighbor triggered*. In the used configuration, each self triggered channel has two neighbor triggered channels. If two self triggered channels are neighbors, they are *self and neighbor triggered*. The trigger information is stored in the hit and is called *trigger type*. All possible trigger types are listed in Table 3.1.

If a second signal occurs on an already triggered pad, the corresponding SPADIC channel gets retriggered and it finishes the first signal. It is called a *multihit*, see Figure 3.12. Message loss can occur due to memory overflow. The information about the end of the message is stored in the *stop-type*, see Table 3.2.

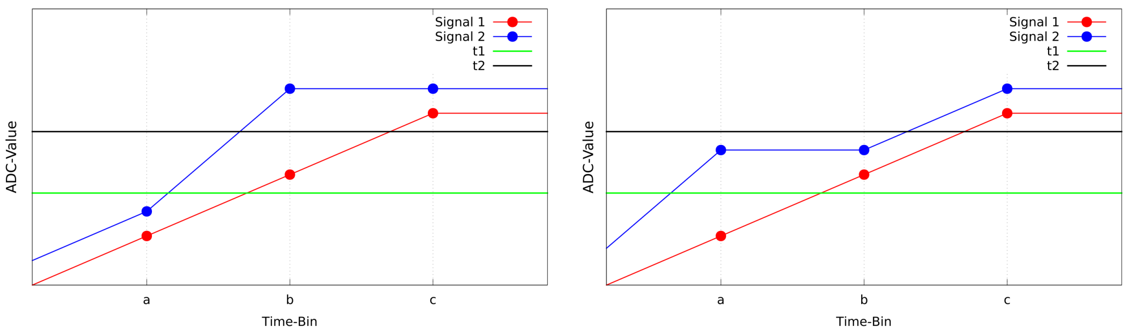

Figure 3.11: a, b, and c are three succeeding time bins. All signals fulfill the condition shown in Equation 3.5. [MA16][edited]

Table 3.1: A list of the possible trigger types is given. The trigger type 0 was not used at the testbeam at DESY in 2017. Information are taken from the SPADIC data sheet. [Kri14]

trigger type	Description
0	global-triggered
1	self-triggered
2	neighbor-triggered
3	self and neighbor-triggered

Table 3.2: A list of the possible stop types is shown. The information are taken from the SPADIC data sheet. [Kri14]

stop type	Description
0	normal end
1	aborted, output buffer full
2	aborted, ordering FIFO full
3	multi hit
4	output buffer full and multi hit
5	ordering FIFO full and multi hit

3.4.2 DAQ-Chain

The used DAQ-chain (*Data AQuisition chain*) consists of the SPADIC 2.0, an AFCK (*AMC FMC Carrier Kintex*), and a FLIB-card (*FLES Interface Board*). The SPADIC generates the pulses from incoming charge, digitizes and sends the messages. In general, the AFCK aggregates up the data of up to three SPADICs and packs the data in the target formate for the FLIB, which is a FLIM link. The AFCK delivers the data to the FLIB card in the computer which writes the data into tsa (*Time Slice Archive*) files. A tsa file is collecting the generated message containers *time slices*. The length of a time slice of data stream was set to 0.1024 s here.

Figure 3.12: Two idealized signals which fulfill the trigger condition. The first puls gets the stop type 3. [K+17]

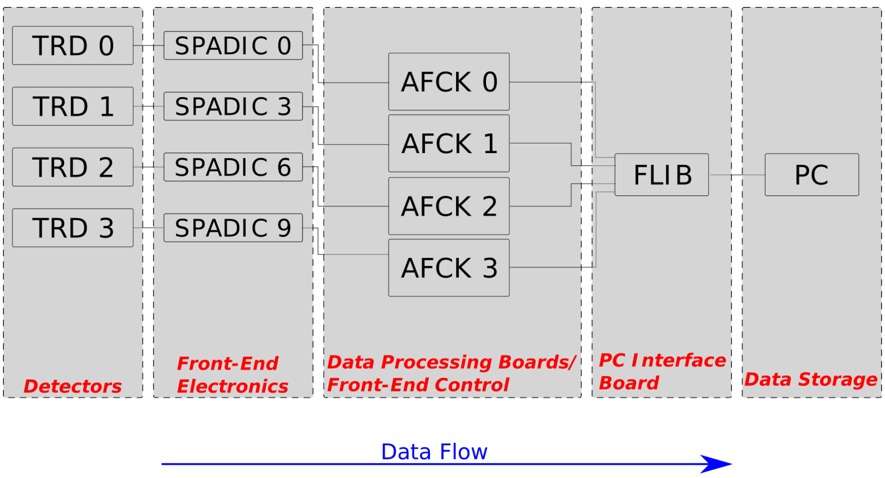

Figure 3.13: Scheme of the DAQ-chain which was used at the DESY 2017 Testbeam. Electronics of detectors which were not used are omitted. The data flow succeds from the left to the right. [MA19][edited]

4 Gas System for the CBM-TRD Prototypes

4.1 Requirements for the Gas System

The detector prototypes need to be supplied with a gas mixture of Xenon and Carbon dioxide. This gas composition has to fulfill high quality standards. These are a high purity, an exact composition of 80 % Xenon and 20 % Carbon dioxide, and a maximum relative overpressure of 1 mbar with a typical flow rate of 3 l/h. The gas condition at the outlet of the detectors should be monitorable to ensure a low contamination, especially during the first flushing procedure after a contamination of the chambers. A small supply system for the detector prototypes was build. It is constructed of two separate sections, a mixing station to provide the detector with gas and an analysis station which monitors the gas properties. For practical reasons, these stations are movable so that they can be used at test beam campaigns just as well as in the local laboratory.

4.1.1 Components

Flow Controller. Due to the fact that the main function of the gas system is to control gas flux, the centerpiece of the system is the flow controller. Flow controllers of two different types of the Vögtlin red-y series were built in. The first model is a single flow controller which steers one gas line, the second is a double flow controller system with two gas inlets, a mixing volume and a combined outlet for the mixed gas. A picture of the double controller is shown in Figure 4.1.
The double flow controllers are calibrated to noble gases (Xenon or Argon) and Carbon dioxide. The single flow controller is calibrated to Xenon, too, but can also be used e.g for premixed gas. In the latter case, calibration conversions are to be applied, which are available for the different gases in the manual for the Aalborg flow meter, whose measurement principle is similar to the read-y flow controller. The controller can be steered by a Modbus protocol with an RS-485 serial connector. The gas flux is derived from the heat flux measurement. A heat source slightly increases the temperature of the floating gas and two temperature sensors are symmetrically placed up and down stream to the heat source in the gas flux. If there is no gas flow, the measured temperature difference between the two readout points is zero. If the gas is flowing, the flux can be determined by the measured temperature difference, see Figure 4.2. This measurement method has the advantage of a low flow resistance but, on the other hand, it is very sensitive to the heat capacity of the gas mixture.

Figure 4.1: The Vögtlin red-y double flow controller is shown. The red boxes are the main flow controllers. On the right side the serial connectors can be seen. The gray block on the left side is the mixing volume. The connected mounting point is tightened with Teflon tape. A display on each controller shows the adjusted gas flux and the applied gas calibration is hand written on the controller.

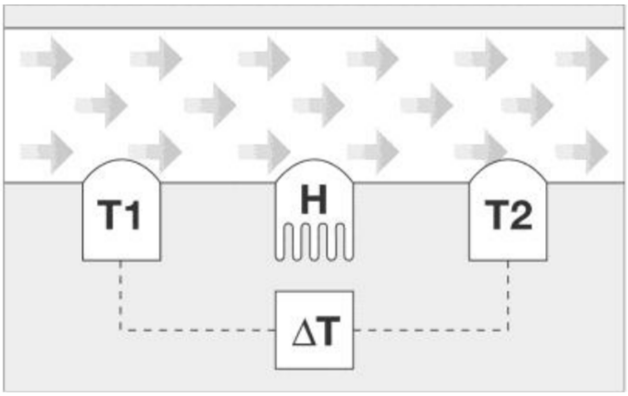

Figure 4.2: The working principle of the flux measurement is sketched. The heater in the middle heats the gas. The temperature sensors measures the temperature. Using the temperature difference, the gas flow is determined. [voe12]

Oxygen Sensor. To ensure that the gas condition in the detectors is in the expected range throughout the experiment, the gas quality has to be monitored. Since the supplied gas has a known composition, the Oxygen contamination is a good indicator for impurities. Elevated Oxygen levels may represent either residuals from the flushing process or impurities due to gas leakage. Oxygen monitoring was conducted using the Orbisphere Oxygen sensor by Hach. Two different models were used, a chemical Oxygen sensor and a sensor with an optical-based measurement principle. The working process of the chemical Oxygen sensor is based on electrolysis. At low Oxygen levels, both sensors perform at the same level of uncertainty.
To measure the Oxygen content applying the optical method, the gas is fed in into the measurement chamber of the optical sensor, as shown in Figure 4.4. The sensor head is made of a luminescent material, whose atomic energy levels are affected by nearby Oxygen. The luminiscent material is illuminated with blue light. To detect shifts of the energy levels caused by Oxygen presence, the emitted light is measured, see Figure 4.3. The Oxygen content is reconstructable from the detected red light.

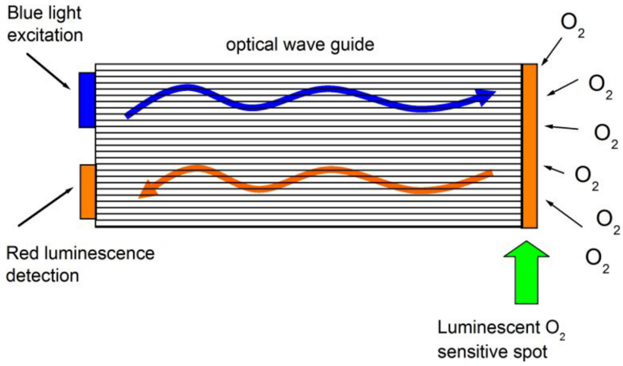

Figure 4.3: A schematic sketch of the optical Orbisphere sensor is shown. On the left side, the blue light gets emitted and excites the optical sensitive molecules. The shifted red light is detected by a detector on the left side [Hac].

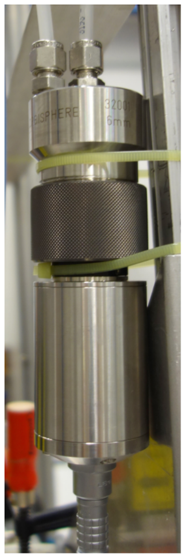

Figure 4.4: A picture of the sensor of the optical Orbisphere. The sensor has to be mounted upright. At the upper side of the picture, the valve mounting points can be seen.

For the sake of completeness, the remaining parts will be listed and shortly described.

Hand Valve. The hand valve was chosen over the electric valve because it enables the user to have the possibility to close single support lines independently of computers or electricity.

Hand Flow Controller. The hand flow controller regulates the flow in each line and is not remote controllable. Due to the fact that during measurements no changes in the flow will be made, a constant flow setting is sufficient.

Flow Meter. An Aalborg GFC flow meter was installed. The principle of measurement operation is similar to the one used in the Vögtlin controllers. It has a $4 - 20\,\mathrm{mA}$ interface.

Bubbler. The bubbler is basically a dead-end tube which is dipping in vacuum oil. The hydrostatic pressure of the oil determines the maximum overpressure in the system at which the gas starts bubbling out. Thereby it is acting as an overpressure fuse.

Pressure Sensor. The differential pressure sensor has a bendable membrane which has changing resistance dependent on the deformation. The sensor has a $4 - 20\,\mathrm{mA}$ interface. It covers a differential pressures range between $-10\,\mathrm{mbar}$ and $+10\,\mathrm{mbar}$. Slightly higher pressure differences are not damaging the sensor.

Moisture Sensor. For humidity measurements, the Moisture Monitor Series 35, Single-Channel Hygrometer was used. To determine the humidity in the gas, the resistance of a porous Aluminum Oxide strip is measured. The sensor has a serial connector, and a standard current and a voltage interface.

All tubing has been done using stainless steel tubes, all tube mounting has been done using the Swagelok mounting system.

4.2 Mixing Station

The mixing station has three gas inlets. One is used for pure Xenon or Argon, one for pure Carbon dioxide, and one for premixed gas. This offers the option to either mix an individual gas composition or to use an already mixed gas circumventing the necessity to recalibrate the flow controllers. In addition, this setup simplifies the handling of the different gases. The differential pressure at the inlet has to remain between 1 bar and 3 bar [voe12]. A pressure reducer at the gas bottle regulates the pressure. All supplied gases have a purity of 4.6.

The mixed gas supplies four different lines each of which has an individual flow regulation. Each line consists of a hand flow controller, a bubbler to prevent overpressure, an Aalborg GFC flow meter to measure the flow, and a hand valve to close inactive lines, see Figure 4.5. This construction offers the possibility to provide up to four gas lines with a stable gas flow using only one flow controller system.

The system is mounted on a 19 Inch Aluminum plate which is mounted in a 16 U (height unit) rack. The design finalisation and mounting were done by Daniel Bonaventura. A photographic rendering of the system is shown in Figure 4.6.

A pressure reducer at the gas bottle regulates the pressure.

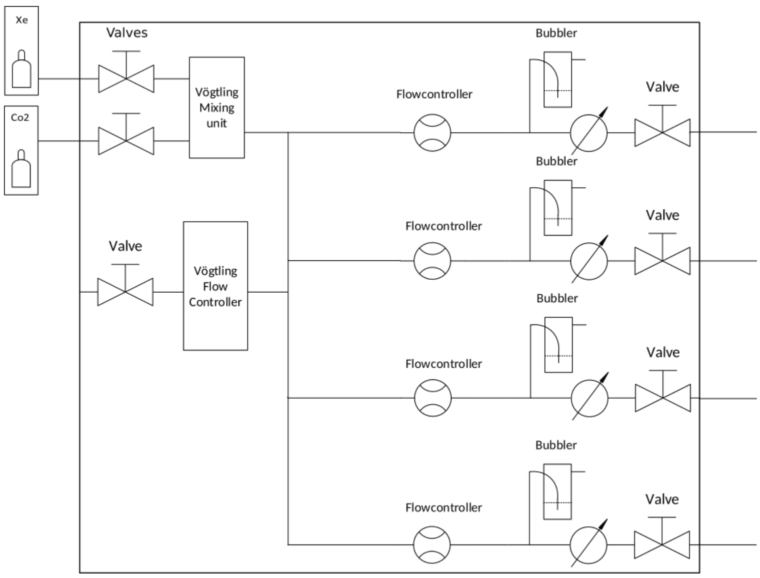

Figure 4.5: A flow chart of the mixing station is shown. On the left side, the gas bottles are connected to the system. The flow controllers adjust the total gas flow in the system and this flow is split to the four support lines. In each line, a hand tunable flow controller, a bubbler, a flow meter and a closing valve is built in.

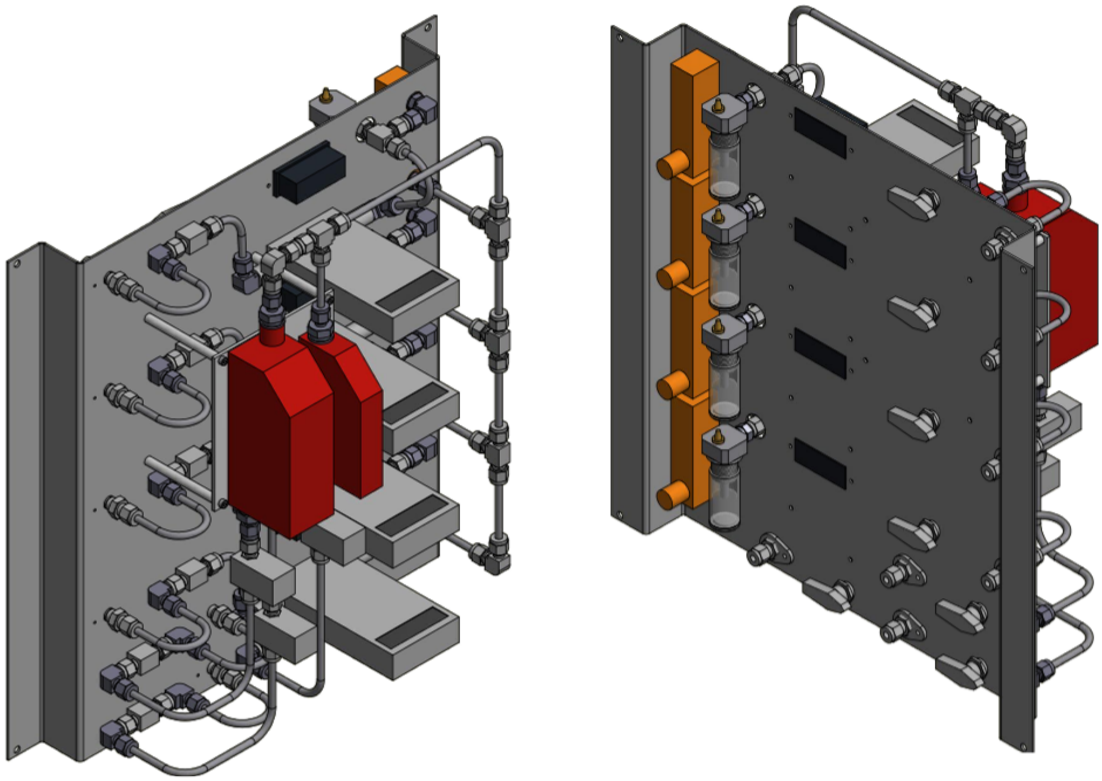

Figure 4.6: The mixing station shown as CAD . The left figure shows the backside with the tubing of the system, the red item represents the flow controllers. On the right, the front side with the gas in- and outlets and the hand valves of the Aluminum plate is shown. The orange items are the hand flow controllers and the black blocks are digital displays of the build in flow meters. The lines are orientated horizontally. Designed by D. Bonaventura.

4.3 Analysis Station

The first part in each line is the bubbler. It is implemented as close as possible to the detectors to minimize the risk of inadvertent high pressure in the chambers. One line is equipped with an additional differential pressure sensor to monitor the differential pressure in this gas line. Each line comes with an Orbisphere Oxygen sensor and a switchable outlet: One is a direct gas outlet, the other one feeds the gas in to a humidity sensor. This is done by implementing a not closable three way valve which offers the possibility to monitor the humidity content of the gas of one single line or of a composition of gas lines. In designing the system, it was of upmost importance to avoid backpressure on the detectors due to accidential closing of the lines. A flow chart of the system is shown in Figure 4.7.
Due to the fact that the Oxygen sensors are not only used at the test beam but also in other laboratory measurements, the sensors can be easily removed.

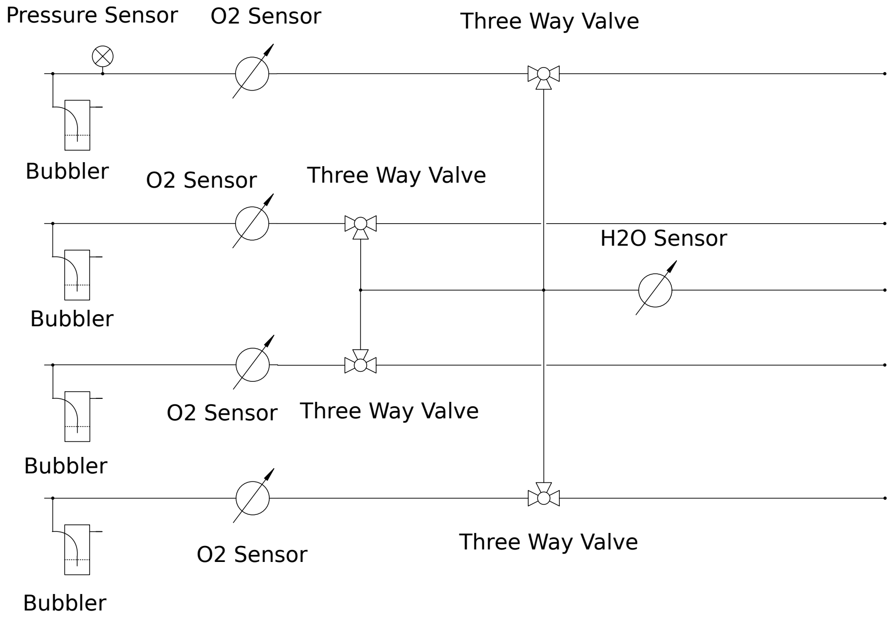

Figure 4.7: The flow plan of the analysis station is shown. Each line consists of a bubbler and an Oxygen sensor and is switchable to a moisture sensor. One of the lines is equipped with an additional pressure sensor.

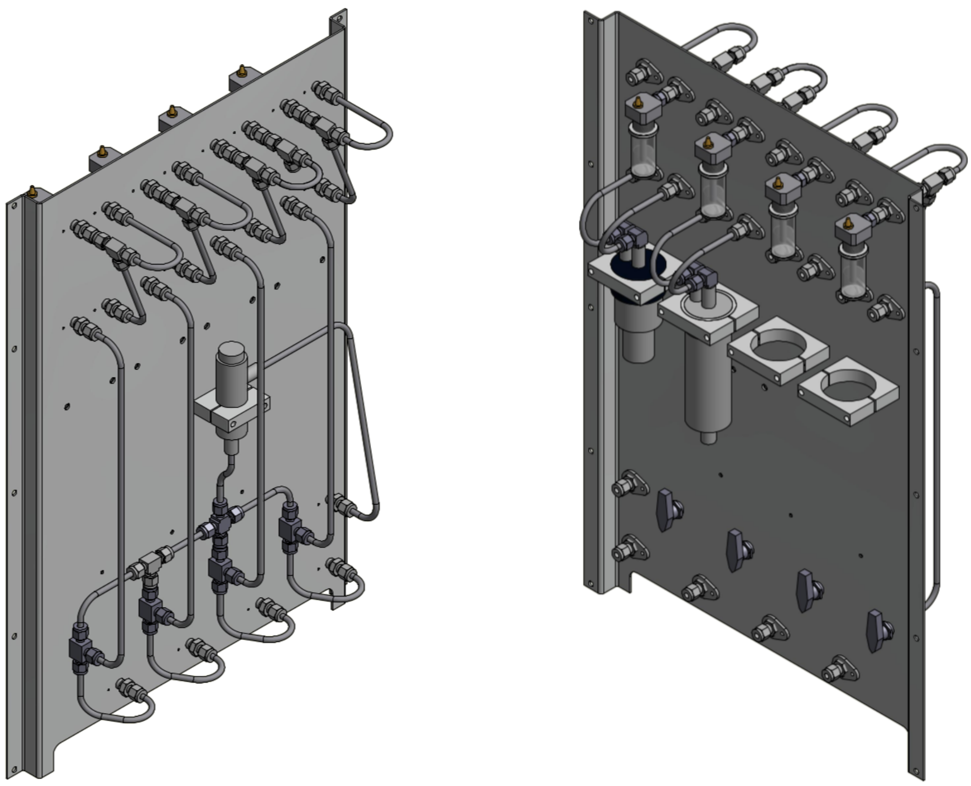

Figure 4.8: This figure shows the CAD from the front (right) and back (left) side of the analysis system. The tubing and the moisture sensor can be seen on the left side. On the right, the front side is shown with the hand wheels and the mounting points for the Oxygen sensors. Designed by Daniel Bonaventura.

4.4 Modification of the Gas Stations

The first versions of the gas system have been tested at a test beam campaign in 2016 at the SPS, at a test beam campaign at DESY in 2017, at a test beam campaign at GIF^{++} in 2017, and in the laboratory. After that, several improvements and changes have been introduced and the system has been optimized for the use at the mCBM campaign at the GSI. In particular, the number of gas lines has been reduced, the systems are, after commissioning, fully remotely controllable and the mounted bubblers have been removed. This enables the system to handle the long supply pipes of the mCBM cave.

4.4.1 Improved Mixing Station

At the mCBM testbeam campaigns, the gas is supplied by gas bottles of pure Xenon or Argon and Carbon dioxide. Thus, only the double flow controller with the mixing unit is used. Each line is closable at the beginning in order to minimize dead volumes in the gas system. Hand flow controllers with a higher sensitivity ($\pm 2.5\,\%$ [Kob18]) were build in and the bubblers have been removed from the stations, but are located directly before the TRDs in the mCBM cave. Due to the long tubing to the cave, the bubblers would not have been sensitive enough for fast pressure changes in the detectors. In addition the high back pressure from the tubing would have been too high for the current models. However, mounting points are preserved. The flow chart of the system is shown in Figure 4.9. The system is built on a new Aluminum plate 4.10.

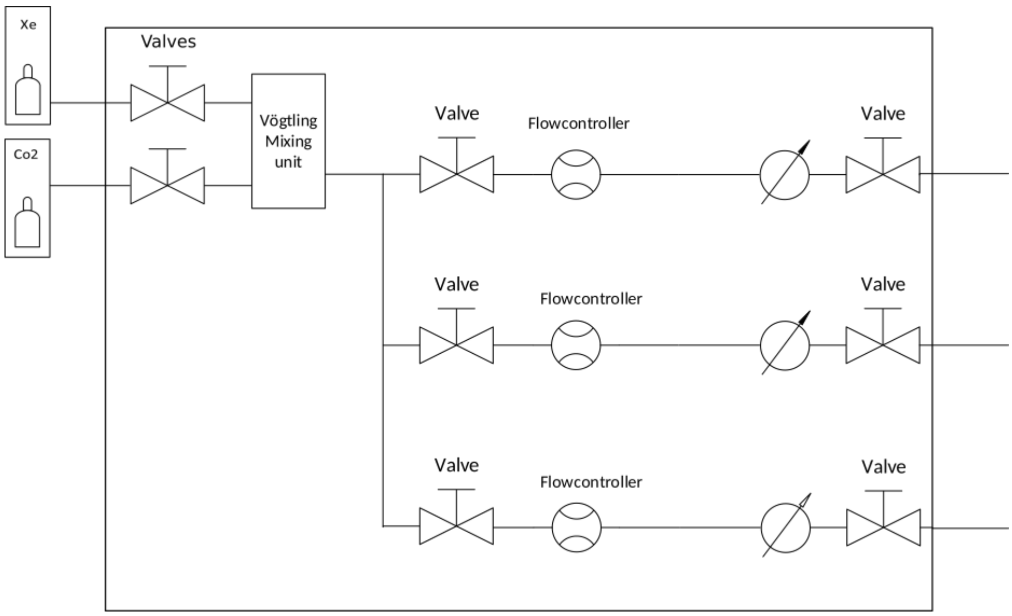

Figure 4.9: The flow chart of the improved mixing station is shown. On the left side, the double flow controller can be seen. The mixed gas is fed into three distinct lines. Each line can be closed individually. In each line, a hand flow controller and a flow meter are built in.

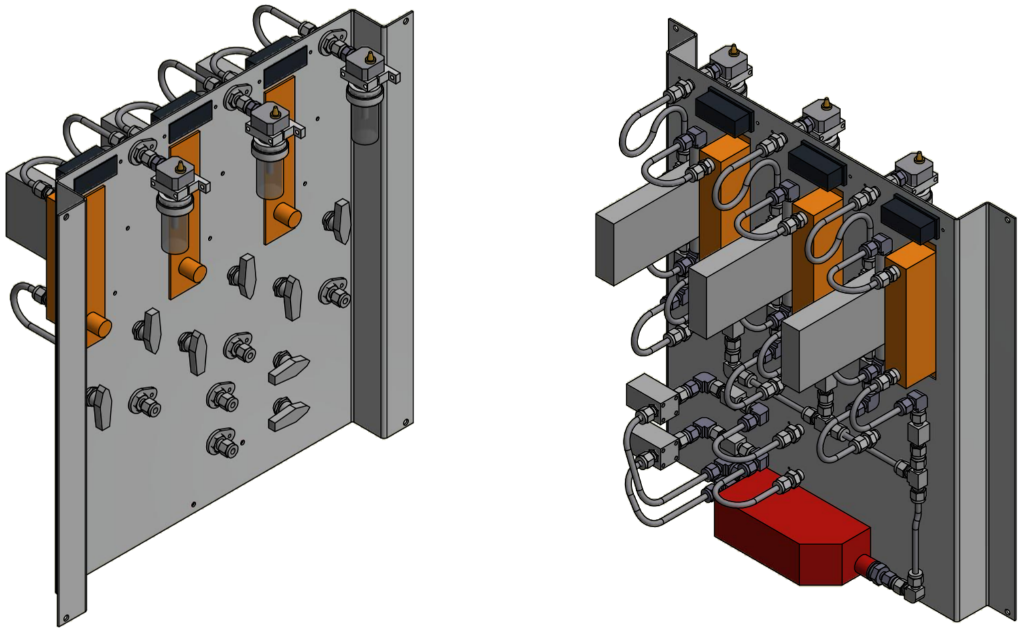

Figure 4.10: The front and the backside of the final version of the mixing station is shown. The orange items are the hand flow controllers and the red box is the double flow controller with the mixing unit. This CAD shows the configuration incorporating bubblers. The lines are orientated vertically. Designed by Daniel Bonaventura.

4.4.2 Improved Analysis Station

For the final implementation to use the analysis station at the mCBM test beam campaigns, the number of analysis lines has been reduced to three. The bubblers were moved from the station to a position in the tubing closeby the detector, see Figure 4.11. However, the mounting points were preserved. Only one Oxygen and one moisture sensor are used in the system. The gas flow of each line can be directed either towards a direct out or to the analysis sensors. Due to the fact that the system is designed for long term test beam campaigns, the sensors can be no longer easily removed. A CAD of the system is shown in Figure 4.12.

4.5 Readout of the Gas System

To read out the sensors and steer the gas flow, a computer is mounted in the mixing station rack. The analysis station is connected to the computer via a *raspberry pi* single-board computer. The digitization of analog signals is implemented using Arduino Uno single-board microcontrollers. The programming of the steering and readout classes was conducted by P. Munkes.

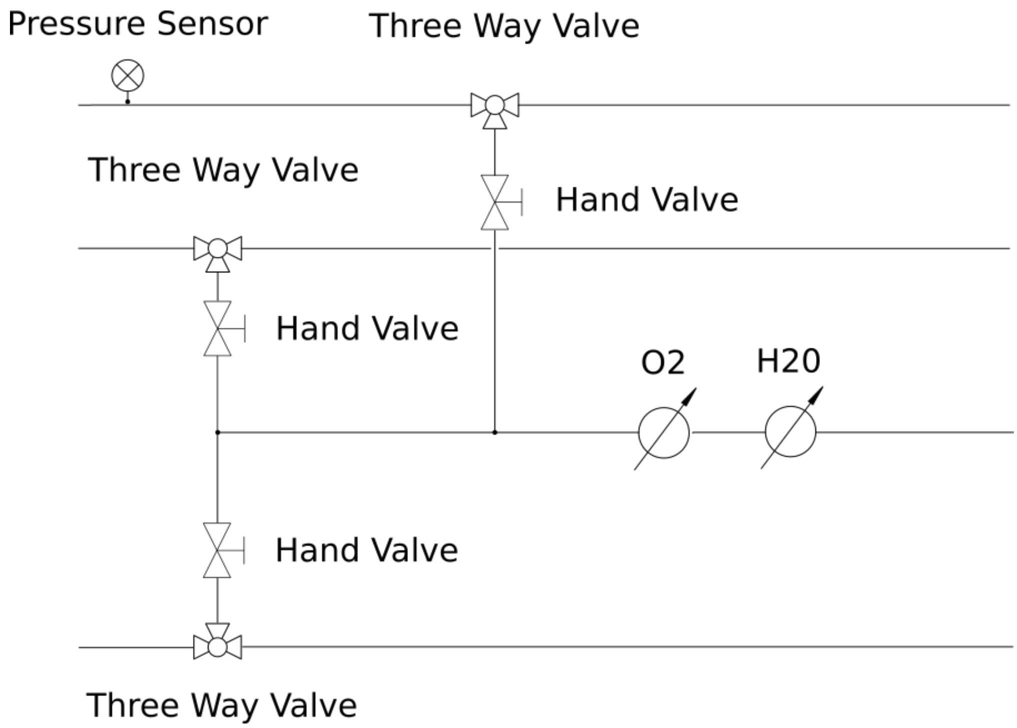

Figure 4.11: The flow plan of the final analysis station is shown. Each line can be directed to the analysis line or to the direct outlet. Between the three way valves and the analysis sensors, additional hand valves has been build in, to reduce the dead volumes in the system.

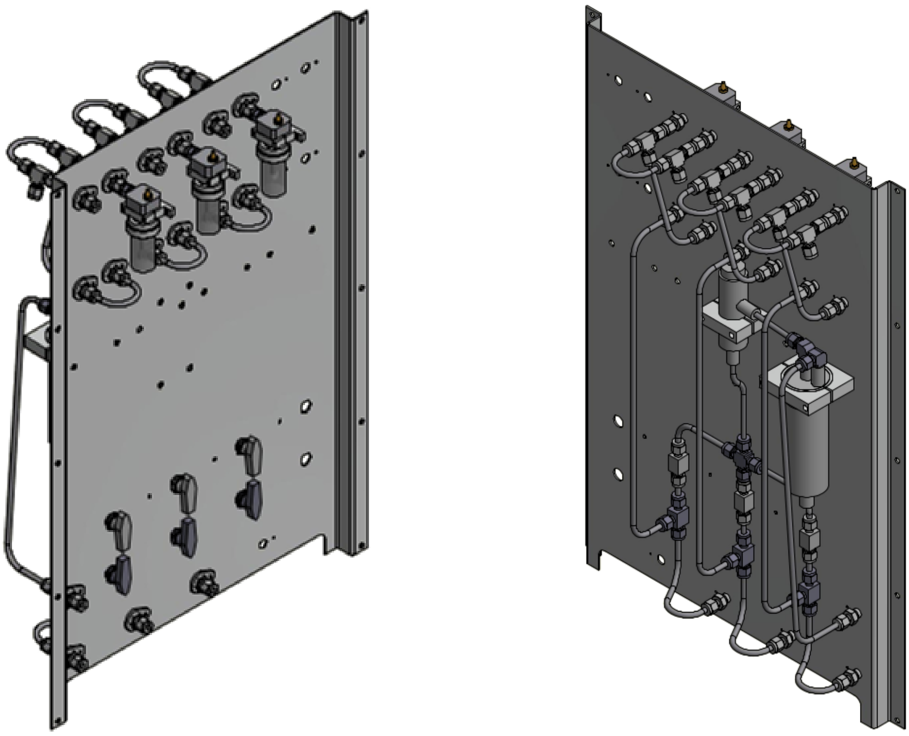

Figure 4.12: The CAD of the final analysis station is shown. The lines are arranged vertically. This CAD shows the configuration with the mounted bubblers. Designed by Daniel Bonaventura.

5 Simulations and Calculations

5.1 Phase Shift

The sampling time of the SPADIC 2.0 is set to 62.5 ns and each shape is segmented in up to 32 samples. For time reconstruction, the exact time position of the analogue pulse has to be reconstructed from the transmitted samples. The proportions of the samples to each other carry this information. For implementation of this time determination, simulations have been carried out. In this analysis, the charge distribution in time is only described with the formula of the shaper, see Equation 3.4.

5.1.1 Shapes at DESY and Future Measurements

Primarily, the unshifted shape has to be defined. It is chosen such that it starts at the beginning of the first bin. So the unshifted shape has the highest possible value for the first bin at a phasing of 0. This shape is shifted to the third sample, since the real shapes are also taken with two *presamples* and the shape is moved to smaller time values by adding the time shift to the unshifted time value. The SPADIC 2.0 has a shaping time of $\tau = 240\,\text{ns}$. The current SPADIC 2.2 has the possibility to switch between a shaping time of $\tau = 240\,\text{ns}$ and $\tau = 120\,\text{ns}$. The shaping time of $\tau = 240\,\text{ns}$ used at DESY is shown in Figure 5.1. As the usage of the $\tau = 120\,\text{ns}$ is foreseen for the experiment, this setting is used in the following calculations. This shape is shown in Figure 5.2.

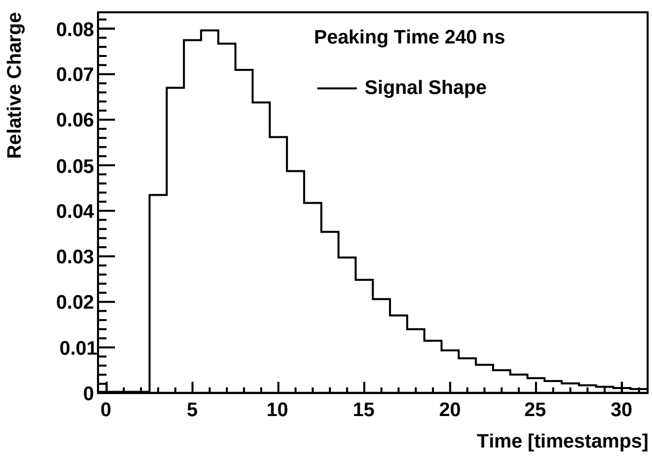

Figure 5.1: A plot of the shape with $\tau = 240\,\text{ns}$ is shown. The peak is broad and and has a long tail.

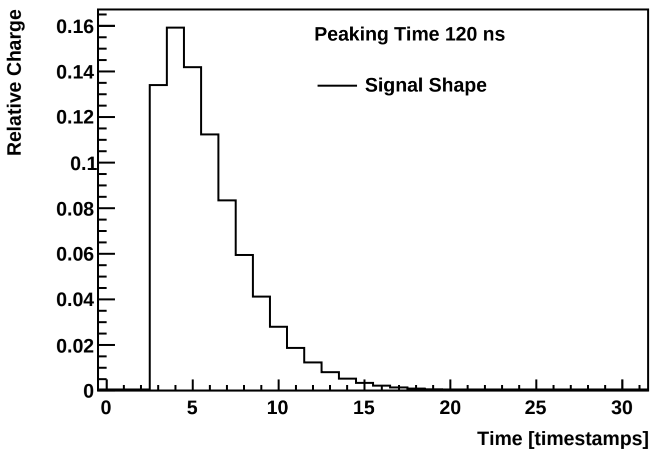

Figure 5.2: A plot of the shape with $\tau = 120\,\text{ns}$ is shown. The peak is much sharper than the peak for the longer shaping time.

5.1.2 Determination of the Phase Shift

Since the shaping time of $\tau = 120\,\text{ns}$ is favored, the phase shift will be discussed with this shaping time, but the principle for the shaping time of $\tau = 240\,\text{ns}$ is the same.
For example, the shapes shifted by 0.3 timestamps (Figure 5.3) and 0.6 timestamps (Figure 5.4) are shown. The examinations have been carried out with phasing steps of 0.1 timestamps. The phaseshift changes the proportions of the bin contents and position of the maximum. The position of the maximum switches between a phase shift of 0.4 and 0.5.

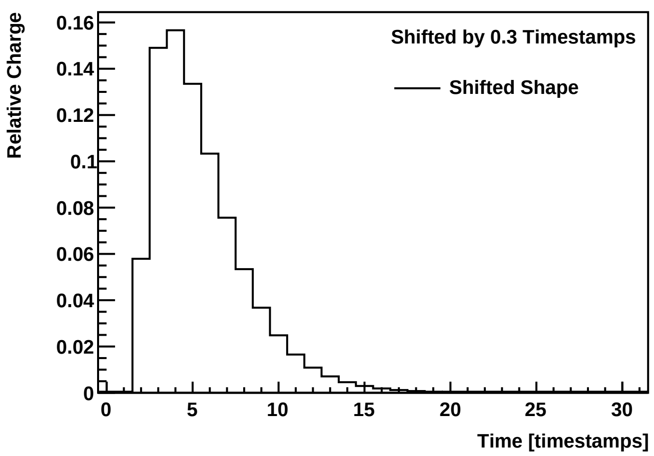

Figure 5.3: The shape with a phaseshift of 0.3 timestamps is shown. In contrast to the unshifted shape, two samples before the maximum have values unequal 0.

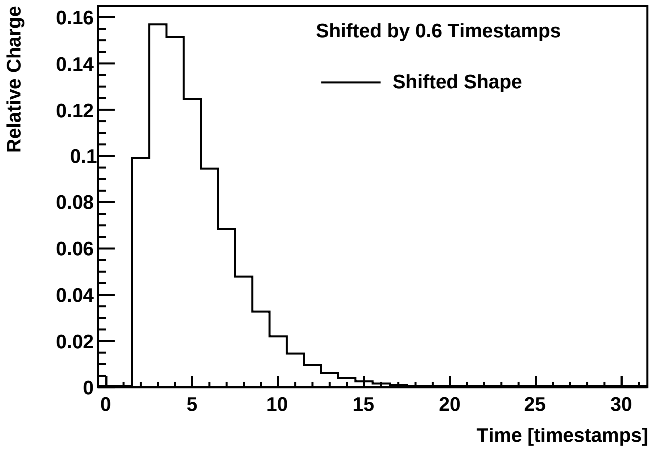

Figure 5.4: This plot shows the shape with a shift of 0.6 timestamps. The maximum has shifted from the 4th timestamp to the 3th timestamp. From this follows, that there is again only one sample unequal 0 before the maximum.

To determine the phasing, a criterion independent of the pulse height has to be used. Due to this, the whole shape is normalized by the ADC value of the maximum. In this simple model, the phase information is stored in each sample and can be calculated by the ratio to the maximum. Since real data have a finite resolution, the samples with the highest values were analyzed to get a stable criterion. The relative height of the sample directly in front of the maximum for the different phasings is shown in Figure 5.5.

The relative height is continuously increasing for higher phase shifts except between the phase shift of 0.4 and 0.5 where the position of the maximum changes. The change in height of the sample two before the maximum is shown in Figure 5.6. Since the position of the maximum changes, not every phasing features a sample two time stamps before the maximum. The relative height of the first sample behind the maximum is shown in Figure 5.7.

These calculations are strongly simplified and do not take noise and smearing effects into account. At real data, the baseline has to be determined and a sample without content does not appear. In addition to that, the trigger condition has to be taken into account, which influences the position of the maximum.

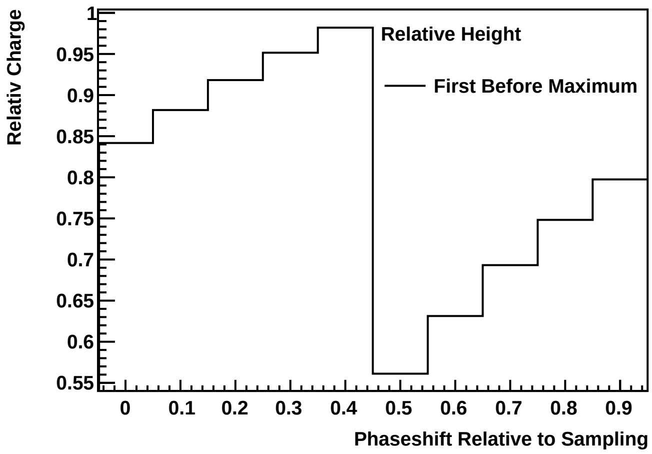

Figure 5.5: The relative height of the sample before the maximum is shown. The position switch of the maximum is the reason for the gap between the phase shift of 0.4 and 0.5. The total variance stays below 0.5, the variance between the different phasings is small and varies.

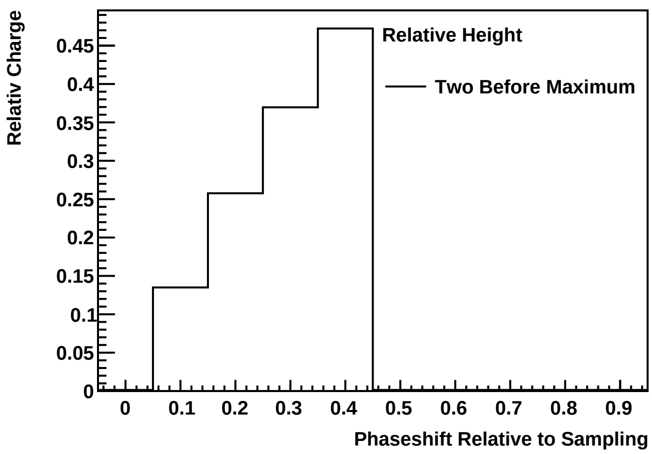

Figure 5.6: The relative height of the sample two before the maximum is shown. Due to the fact that the position of the maximum is changing in dependence of the phase, a sample two before the maximum does not exist at every phasing.

5.1.3 Charge Calculation

To estimate the height of a pulse of a particle with a given energy, the charge creation in the detection material and the charge per ADU (*Analog Digital Unit*) has to be calculated. The outcome of a pulse of 10 fc at the ADC is 187 mV for the FG (*Full Gain*) configuration of the amplifier and 99 mV for the HG (*Half Gain*) configuration [Fis]. The ADC has an input range of 960 mV [Fis] which is separated in 512 ADU, that leads to a translation of 1.875 mv/ADU. The charge per ADU is 0.10027 fC/ADU or 625.83 e/ADU for FG and 0.18939 fC/ADU or 1182.08 e/ADU for HG.
The charge which is seen by the shaper of the SPADIC after an event in the detection gas took place

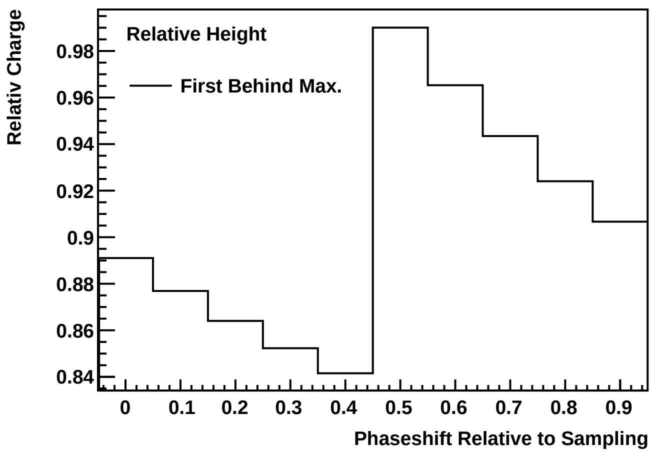

Figure 5.7: The relative height of the first sample behind the maximum is shown. Due to the fact that the phasing is shifted to lower values, the relative height behind the maximum is decreasing for increasing phasings.

can be calculated via [And20]:

$$PH = Q \cdot G_{gas} \cdot K_{pad} \cdot K_{SPADIC} \cdot G_{SPADIC}. \tag{5.1}$$

Q is the charge deposit for a given process; K_{pad} is the fraction of charge which is seen by the cathode pads, usually between $30 - 40\,\%$, depending on wire geometry; K_{SPADIC} is the fraction of pad charge which is seen by the SPADIC, usually between $30 - 70\,\%$; G_{gas} is the gas gain of the detector, usually adjusted to 2000. The different modes of the SPADIC gain G_{SPADIC} are already described.

Table 5.1: Calculated values for MIP

$K_{SPADIC} \cdot K_{pad}$	Gain	Pulse Height
0.09	FG	78.44 ADU/MIP
0.09	HG	41.52 ADU/MIP
0.175	FG	152.52 ADU/MIP
0.175	HG	80.73 ADU/MIP
0.28	FG	244.04 ADU/MIP
0.28	HG	129.17 ADU/MIP

The created charge can be calculated with the energy deposition in the gas. The energy loss of a MIP (*Minimal Ionizing Particle*) in the used gas mixture of Xenon/Carbon Dioxide 85/15 is about 5 keV/cm [AW12]. Since the gas volume has a thickness of 1.2 cm the mean energy deposition for a MIP particle is 6 keV. The ionization work of Xenon which is needed to ionize one electron is 22 eV[BRR08]. Since the value for K_{SPADIC} varies and the product of K_{pad} and K_{SPADIC} is not well known, calculations for minimal, maximal and the middle value of the product of K_{SPADIC} and K_{pad} have been done. The results are shown in Table 5.1. Taking those calculations into account, minimal trigger thresholds can be estimated.

5.2 Position Reconstruction

To test the position reconstruction algorithms, the charge distribution on the pads can be calculated with the Mathieson formula. This formula is given in Equation 3.1. The distributed charge is normalized and the distance to the cluster center is called displacement and measured in pad length. This yields the possibility to adapt the calculations to different rectangular pad geometries. Figure 5.8 shows the charge which would be measured on the pads in case of a symmetrical 3-pad cluster and Figure 5.9 shows the charge in the case of a symmetrical 4-pad cluster. A 4-pad cluster consists of 4 pads and arises mainly when a hit occurs nearby a pad border.

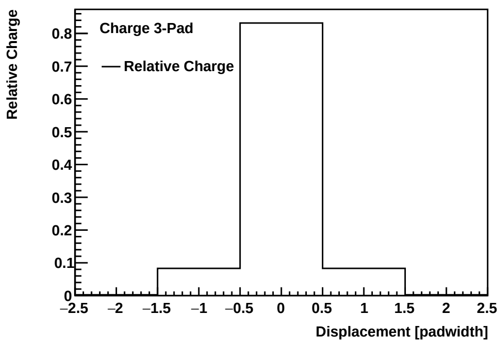

Figure 5.8: The measurable charge of a 3-pad cluster is shown, which occurs at the center of a pad. 83.17 % of the charge is located on the central pad while the neighbor pads hold 8.31 % each. A symmetrical 3-pad cluster contains 99.79 % of the charge.

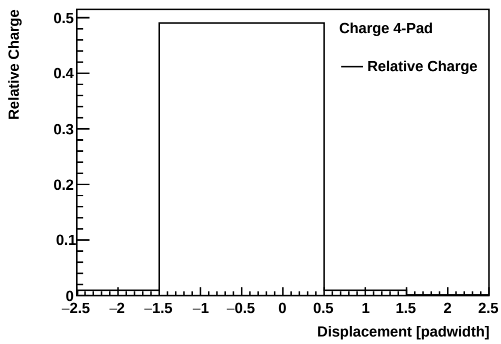

Figure 5.9: The measurable charge of a 4-pad cluster is shown, which occurs at a pad boarder. The central pads carry 49.04 % of the charge each, the neighbors 0.95 % of the charge each. For analytical reasons, one of the central pads has to be defined as the central pads with a displacement of 0. A symmetrical 4-pad cluster contains 99.97 % of the charge.

5.2.1 3-Pad Cluster

For the reconstruction of 3-pad clusters, two different algorithms are available. On the one hand the cog (*center of gravity*) algorithm as described in Formula 3.2 and on the other hand the sech (*secant hyperbolic squared*) method as described in Formula 3.3. To test the algorithms, the charge distribution is simulated with the Mathieson formula and the known center of the charge distribution is shifted step by step by 1/100 pad length. Furthermore the reconstructed cluster center (d_{reco}) is compared to the known cluster center (d_{truth}). For the pad width of 1.25 cm it has a step size of 125 μm. Since the charge distribution is symmetrical to its center, the center of the charge distribution is only shifted from the pad center to the pad border and only in one direction for the three pad clusters. With this shift, all possible charge positions relative to the pad center are covered. The divergences between the given cluster positions and the reconstructed cluster positions are shown in Figure 5.10 for the cog algorithm and in Figure 5.11 for the sech algorithm. In both

cases the d_{reco} is subtracted from the d_{truth}.
Both algorithms tend to induce a slight shift. The displacement reconstructed with the help of the cog algorithm has a maximum shift of 0.381 mm to the given displacement of 1.959 mm. This shift is in the direction of the pad center. The sech algorithm has a shift of -0.245 mm at a given displacement of 1.817 mm. This shift is in the direction towards the pad borders.

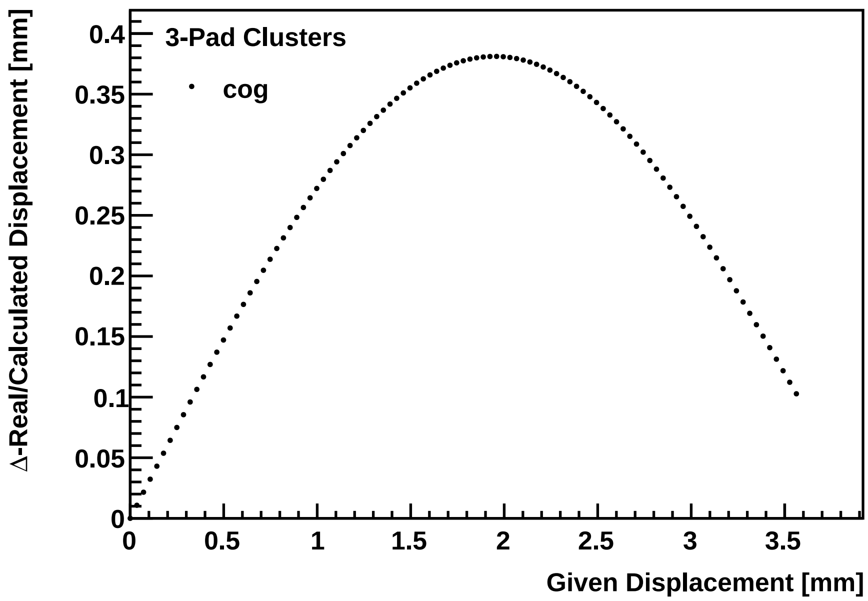

Figure 5.10: The difference between d_{truth} and d_{reco} for the cog algorithm is plotted with the given displacement on the x-axis. The highest difference takes place at a simulated displacement of 1.959 mm with a difference of 0.381 mm which is a shift towards the pad center. The relationship between the calculated difference and the given displacement is similar to a downwards opened parabola. The lowest differences can be found for the lowest and highest values of the given displacements.

With this knowledge, a correction of the reconstructed position can be achieved. In Figure 5.12 the calculated displacement is plotted against the given displacement for the cog algorithm and the sech algorithm. Both algorithms have the highest inaccuracy for a given displacement of roughly 2 mm. Since no tests with real data have been conducted, further investigation and the implementation in the analysis framework has to be done. Since the real position of the hit is not known, a test could not be done in a simple, direct way as it has been done in the present work. Further investigations about the influences of noise on the reconstruction accuracy have to be done.

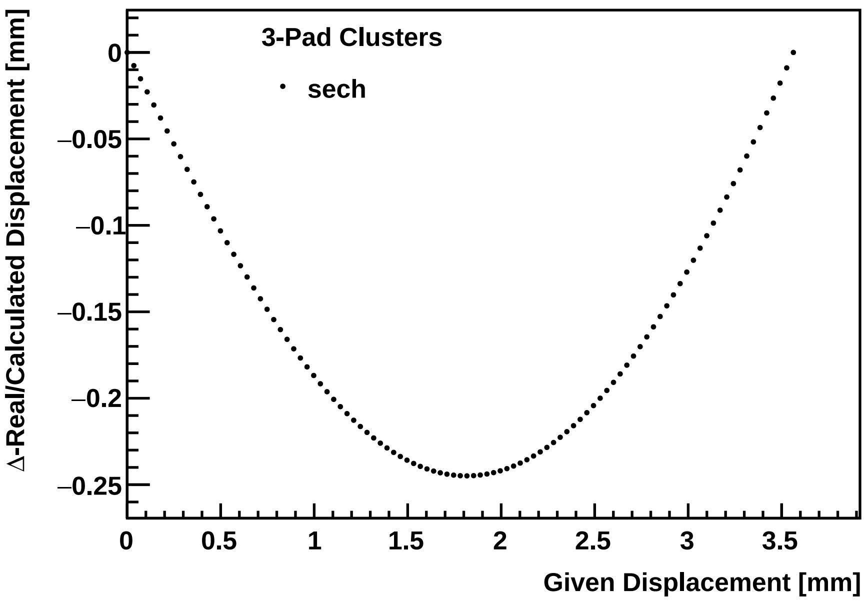

Figure 5.11: The difference between d_{truth} and d_{reco} for the sech algorithm is plotted with the given displacement on the x-axis. The highest difference occurs at a simulated displacement of 1.817 mm with a difference of -0.245 mm which is a shift towards the pad border. The relationship between the calculated difference and the given displacement is similar to an upwards opened parabola. The lowest differences can also be found for the lowest and highest values of the given displacements.

5.2.2 4-Pad Clusters

If a particle hits the detector nearby a pad border, the main part of the induced charge gets distributed on two pads, each of them may fulfill both trigger conditions, *self-* and *neighbor triggered*. In this case, a 4-pad cluster is created, this 4-pad cluster does not have to contain a higher charge than a 3-pad cluster. The sech algorithm is not able to deal with other clusters than a 3-pad cluster. In the case of 4-pad clusters, the center of the charge distribution is only shifted from the pad border to the center of the pad. The accuracy of the 4-pad cog algorithm is shown in Figure 5.13. The biggest aberration takes place at a simulated position of 5.273 mm with a shift of -0.338 mm towards the pad center.

Another reconstruction method for 4-pad clusters has been suggested [Mun16], which is a combination of two sech algorithms. The 4-pad cluster is separated into two 3-pad clusters of which the average is calculated:

$$P_{total} = \frac{P1_{sech} + P2_{sech}}{2}. \tag{5.2}$$

$P1_{sech}$ and $P2_{sech}$ are the with the help of the sech algorithm reconstructed positions of the cluster fractions and P_{total} is the total position of the main cluster. The results of the simulation are shown in Figure 5.14. This reconstruction algorithm does not properly fit the given data. The simulated position of 3.5625 mm can be calculated exactly, but the aberration increases strongly for higher

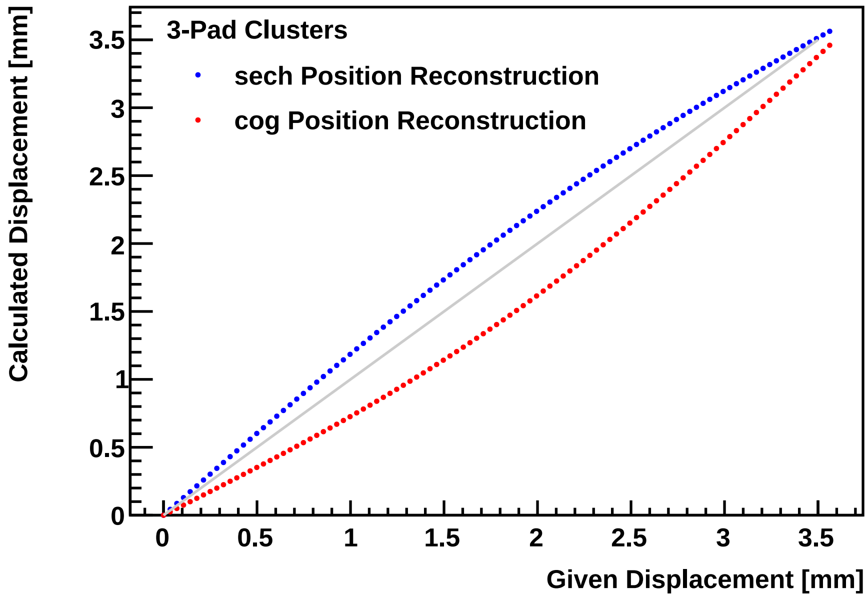

Figure 5.12: The displacements calculated with the sech and the cog algorithm are plotted against the given displacement. To guide the eye, a diagonal which represents a perfect reconstructed position is drawn in. The points differ in a convex form from the linear relationship for the sech algorithm and in concave form in the case of the cog algorithm. The maximal aberration for the sech algorithm is smaller than for the cog algorithm.

simulated displacements. The plot for both corrections is shown in Figure 5.15.
In addition to that, an algorithm with a combination of the sech algorithm (see equation 5.3) and the cog algorithm and a weighted average (see equation 5.4) has been tested. The weighting factors were the charge of the exterior pads of the cluster fragments. The results of those algorithms were also not as precise as the cog-algorithm reconstructions.

$$P_{total} = \frac{P1_{sech} \cdot C1_{sech} + P2_{sech} \cdot C2_{sech}}{C1_{sech} + C2_{sech}} \tag{5.3}$$

$C1_{sech}$ and $C2_{sech}$ are the charges of the cluster fragments.

$$P_{total} = \frac{P1_{sech} \cdot Co1_{sech} + P2_{sech} \cdot Co2_{sech}}{Co1_{sech} + Co2_{sech}} \tag{5.4}$$

$Co1_{sech}$ and $Co2_{sech}$ are the charges of the exterior pads of the cluster fragments.

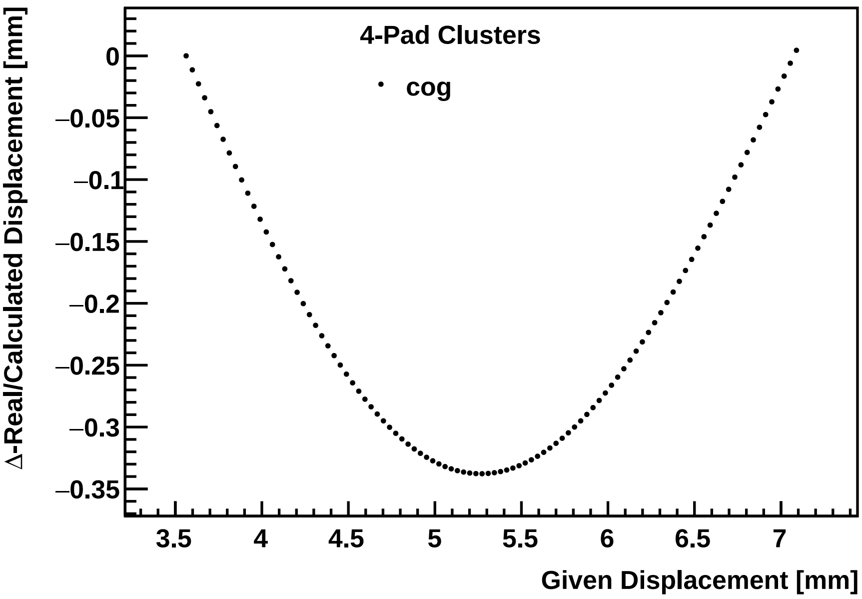

Figure 5.13: The difference of the reconstructed and the given displacement is plotted against the given displacement. The reconstruction has been done with the cog algorithm. Since a symmetric distributed 4-pad cluster has its center on a pad border, the displacement starts at a value of roughly 3.5 mm. The biggest shift is at a given displacement of 5.273 mm with a shift of −0.338 mm. This is a shift towards the pad center.

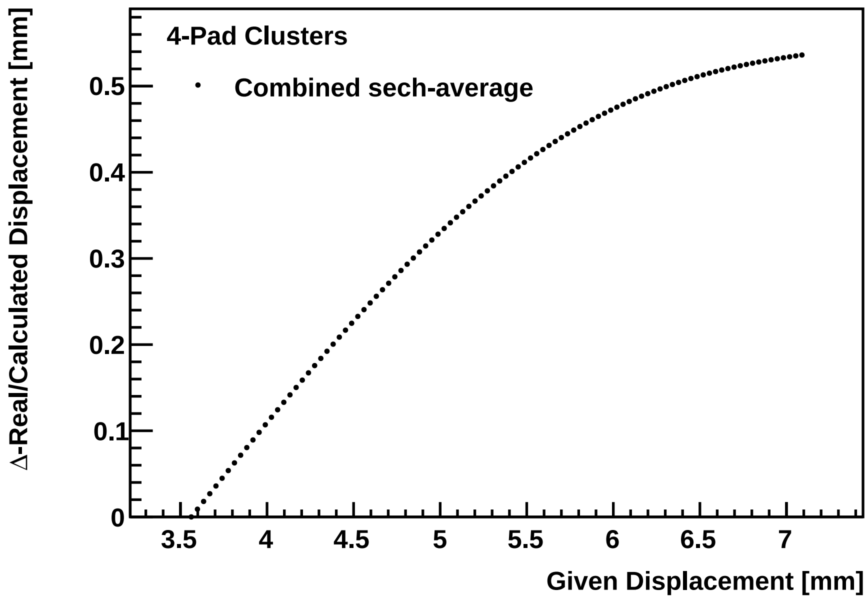

Figure 5.14: The difference of the reconstructed and the given displacement is plotted against the given displacement. The reconstruction has been done with the 4-pad sech algorithm and the reconstructed position differs strongly from the given position. The shape seems to be similar to the translation function of the other algorithms, but it has nothing in common with it, since it should be similar to the shape of the plots as shown in Figure 5.13. The reconstruction for low values is relatively accurate but gets worse for higher values.

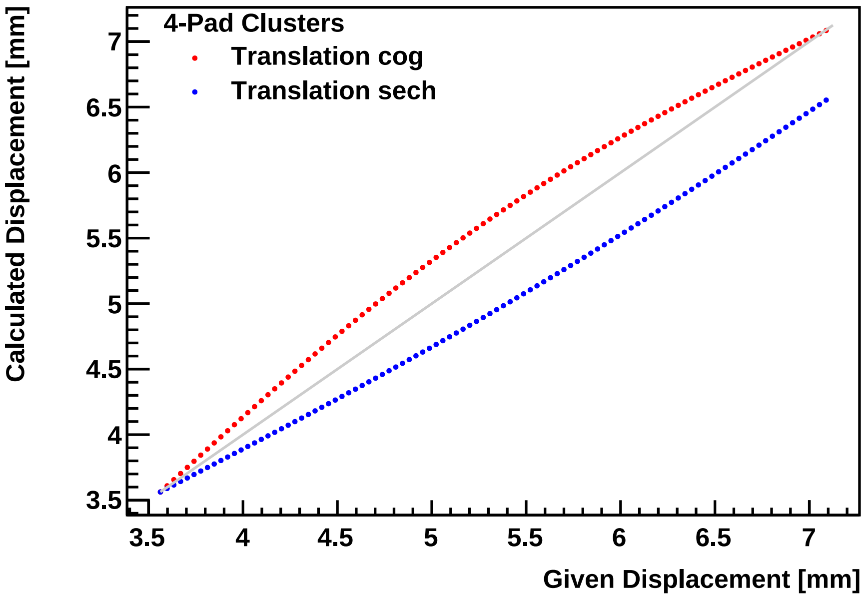

Figure 5.15: The displacements calculated with the combined sech-average and the cog algorithm is plotted against the given displacement. To guide the eye, a diagonal which represents a perfect reconstructed position is drawn in. The points differ in a concave form from the linear relationship for the cog algorithm. The combined algorithm provides good approximations for small displacements but differs strongly for higher given displacements.

6 DESY Testbeam Campaign

In September 2017, a testbeam campaign at the DESY (*Deutsches Elektronen Synchrotron*) facility at Hamburg took place. The facility provided an electron beam with an adjustable beam energy between 1 GeV and 6 GeV [D+18]. At this testbeam campaign, four prototypes of the design described in chapter 3.1.2 were tested. In addition to that, two scintillation detectors and a small 2014 prototype were set up and used as reference detectors. For calibration matters, a Fe^{55} source was installed at the up first prototype in a region distant to the beam spot. The MWPCs were flushed with Xenon/CO_2 in the ratio of 80 /20 . This gas mixture was provided by the described gas system, see chapter 4. Different measurements with and without the radiators described in chapter 3.3 were done. Due to the fact that the focus of the present work is on the position reconstruction and cluster analysis, the radiator configurations are not of a special interest. In the readout chain, the SPADIC 2.0 was used.

6.1 Deutsches Elektronen Synchrotron

The DESY II is a synchrotron accelerator, mainly used to inject electrons/positrons into the larger synchrotrons DORIS or PETRA. It has a total length of 292.8 m and thereby a revolution frequency of about 1 MHz [D+18].

When the accelerator provides the three testbeam areas with electrons/positrons, fiber targets are used to generate high energy bremsstrahlung. This bremsstrahlung irradiates a converter target to produce electron/positron pairs. With a magnet and a collimator, the required electron/positron energy can be selected. A scheme of the electron/positron beam production is shown in Figure 6.1. Different converter targets are available to adjust the desired rate. In this testbeam, a 4 mm copper target was used, to get the highest available electron rates. The different targets were characterized by the DESY testbeam team as shown in Figure 6.2. Energies at the high and the low end of the energy spectrum can be reached but have a lower hit rate.

The test stand contains a final lead collimator to vary the collimation and the illuminated area on the detector. The inserted collimator has a 10 mm $\times$ 10 mm quadratic shape and is shown in Figure 6.3.

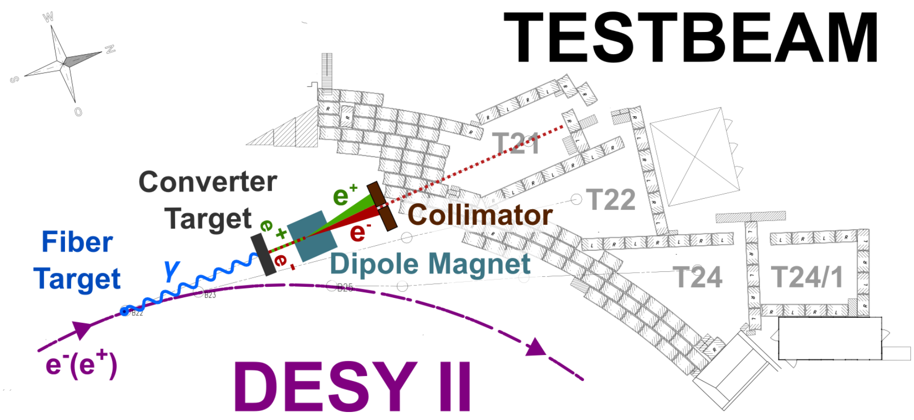

Figure 6.1: A scheme of the DESY II testbeam generation is shown. A fiber target produces bremsstrahlung, this bremsstrahlung produces electron/positron pairs which are selected by a collimator and a magnet. This sketch shows the beam generation for the test stand T21, while the experimental setup was located at test stand T22 with an identical generation scheme [D+18].

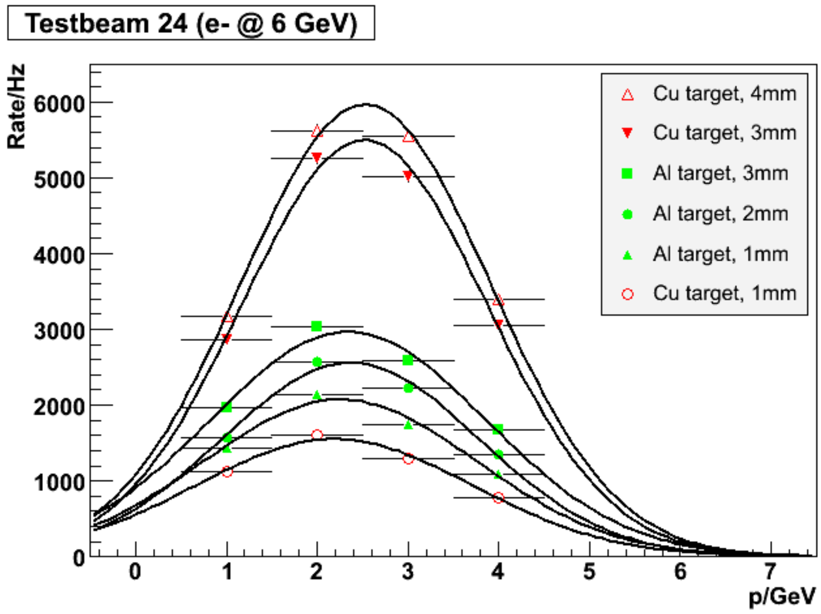

Figure 6.2: The event rate in dependence of the energy of six different converter targets is shown. The used target was a 4 mm copper target, the highest rates are reached for an electron energy of 2 GeV [des17].

6.2 Setup at DESY

At the DESY 2017 testbeam campaign, the four detector layers of the tested prototypes were placed in-line with a distance of 57 cm to each other. Each detector is equipped with a 30 cm foam foil radiator and a SPADIC 2.0 as read-out electronics. The last chamber in the beam line is rotated by 90° to resolve the electron in the axis vertical to the other three MWPCs. The different detector layers are numbered from 0 to 3. The detectors are provided with premixed bottle gas of a composition of

Figure 6.3: The Lead collimator at the test stand T22 is shown. A quadratic hole collimates the beam.

80 % Xenon and 20 % Carbon dioxide and are connected serially. The gas has a purity of 4.6.
A detector of the small 57 cm × 57 cm 2014 prototypes was installed 121 cm behind the last large prototype to use the position information as a reference. A true scale sketch of the final setup is shown in Figure 6.4. This detector was provided with a gas composition of 82 % Argon and 18 % Carbon dioxide with a purity of 4.6. Since this detector was not taken into account in this thesis the detailed description of the pad plane and the specifications get omitted at this place.
The gas quality and purity of the four main detectors and the single reference detector has been monitored by the analysis station at the development status as described in chapter 4.3. The whole setup is shown in Figure 6.5.

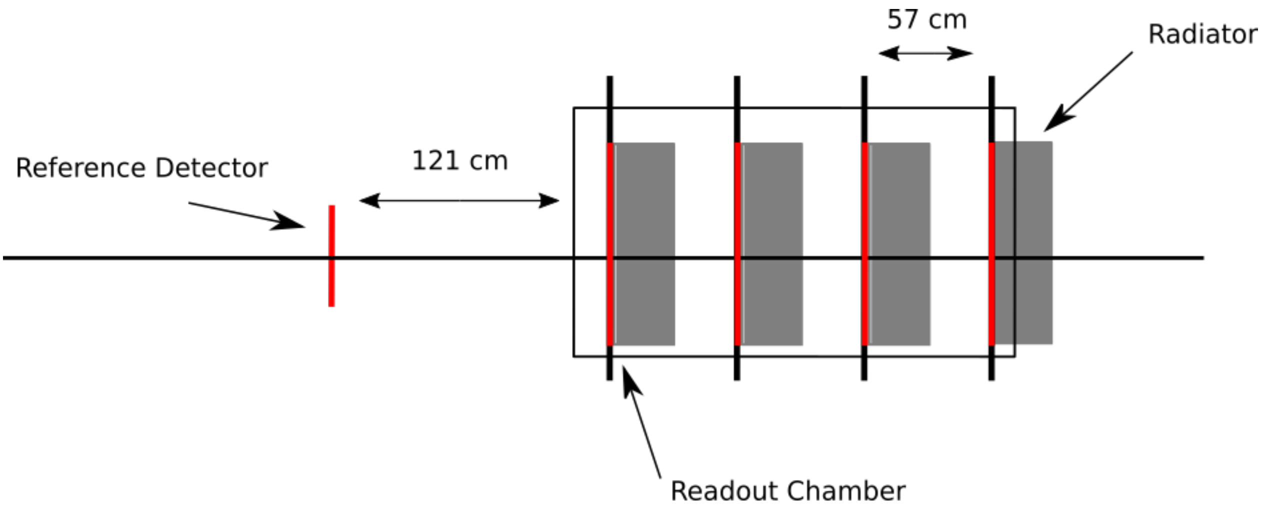

Figure 6.4: A true to scale sketch of the setup installed at the DESY 2017 testbeam campaign is shown. The horizontal black line represents the electron beam and the black lined rectangle the mechanical support structure for the detectors. The lighter gray rectangles represent the radiators, the red lines the detection volume. In this sketch, the electrons pass the detectors from the right side to the left.

Figure 6.5: The front side of the detectors are shown. The white boxes are the radiators, the Fe^{55} source is not mounted at this configuration. The golden entrance window behind the four detectors is the reference chamber. At the bottom left corner, the analysis station can be seen.

7 Analysis

The following research is based on data taken at the testbeam campaign at the DESY testbeam facility in 2017. The electron beam was provided via generation mechanisms by the the DESY II accelerator. Multiple measurements with different electron momenta, rates, and detector adjustments have been done. Due to the fact that the analysis at hand was focused on position reconstruction and the timing of hits, a single run with stable conditions was investigated. Used here was mainly run 111. Other runs have been examined for cross checks, to ensure representative statements. It was made sure that the analyzed data has not been taken at the beginning or ending of a run, to avoid effects of the ending sequence of the electron beam shutter or ramping effects from the beam magnets for momentum selection. At this measurements, the provided electron beam had a momentum of 3 GeV, the anode voltage of the TRD was adjusted to $U_a = 2000\,\mathrm{V}$ and the drift voltage to $U_d = -500\,\mathrm{V}$. The trigger thresholds were set to $th1 = -205\,\mathrm{ADU}$ and $th2 = -180\,\mathrm{ADU}$. The synchronization between the different SPADICs was corrected by the time shift found by A. Meyer-Ahrens [MA19]. The utilized software is the CBMRooT framework at the version of 18 June 2019 with the ROOT version 6.12. [BR].

7.1 Time Structure

To estimate the probability of multi hits, the time between two hits on the same pad is determined and written into a histogram. Only signals of the triggertype 1 (*self triggered*) and 3 (*self and neighbor triggered*) were taken into account, see Figure 7.1.

For small time differences, many signals are counted, for higher time differences a regular pattern is recognizable. To reduce the amount of noise triggers, a filter based on the signal shape has been designed. Either the signal is required to follow the expected rise or the signals maximum ADC value is higher than $-130\,\mathrm{ADU}$ to be taken into account. A rising shape has to fulfill the chosen condition:

$$\text{Shape Condition} = [S_0 < -200] \wedge [S_4 \leq S_5] \wedge [S_4 > -200]. \tag{7.1}$$

S_x is the ADU value at the bin with the number x.

421324 pulses are taken into account; these pulses are shown in Figure 7.2. Many of the pulses reach the maximum of the ADC range and are clipped. This is sufficient for the simple time difference analysis of the hit pad. The total number of rejected pulses is 115144; the rejected pulses are shown in Figure 7.3. 21 % of the signals with trigger type 1 or 3 do not feature the normal shape what makes it probable that it is random noise. Although some correct signals are included, the number of the correctly rejected signals is considerably lower.

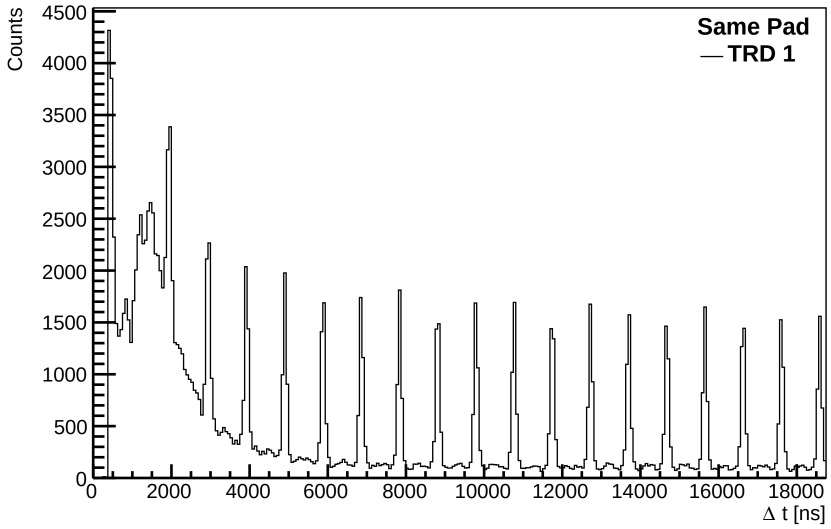

Figure 7.1: The time difference between two hits on the same pad is shown. In the region up to approximately 6000 ns many signals are detected. For higher time differences, a regular pattern can be recognized.

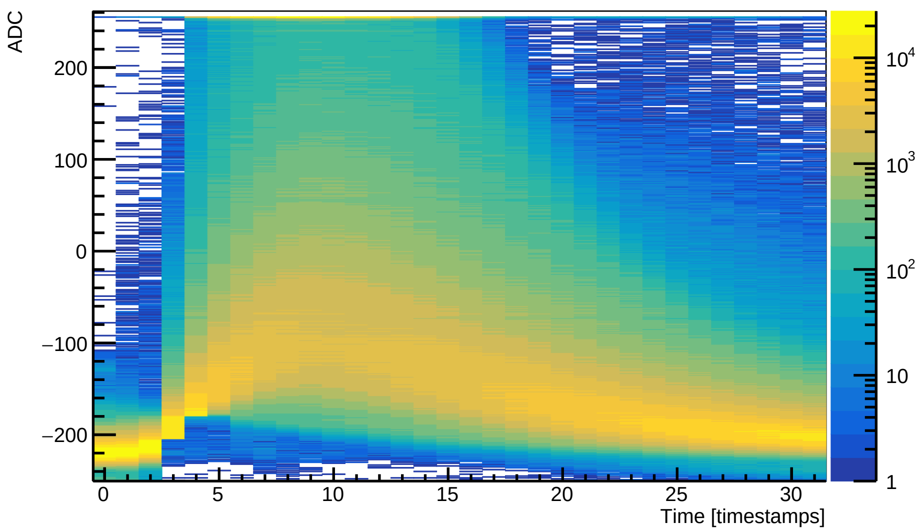

Figure 7.2: The shapes of the pulses used in the time difference investigation are shown. The ADC values are plotted against the time in timestamps. Many of the pulses are clipping at the maximum of the ADC range. The low signals, probably caused by noise, are reduced strongly.

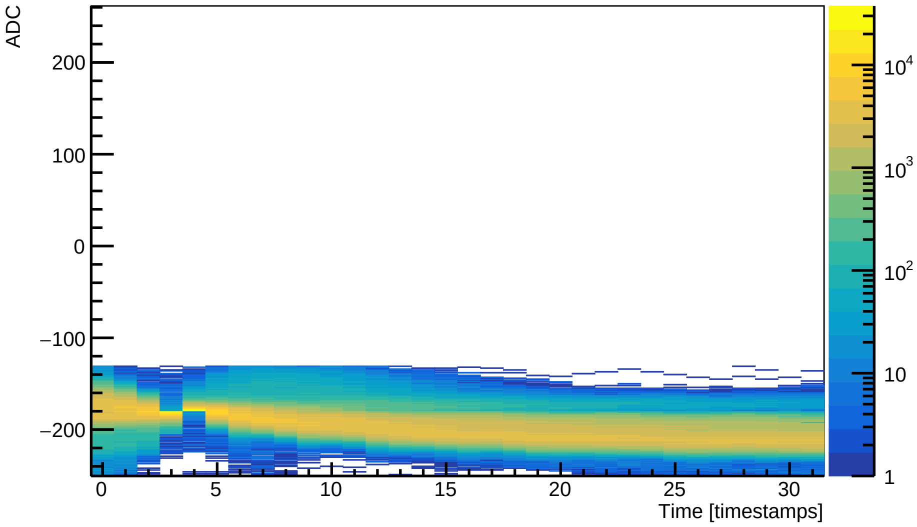

Figure 7.3: The shapes of the rejected pulses are shown. The cut for signals with a maximum value higher than −130 ADU can be seen. Most of the curves do not feature the expected shape.

The time differences at layer 0 is shown in Figure 7.4. The distribution of the time differences shows a periodic pattern. The analysis of the pattern indicates, that it is regularly quantized with a quantization time of 15.64 timestamps which corresponds to 977 ns. This has been calculated by averaging the time of the 100th peak. Since each pulse contains only a low number of entries, the position has been approximated by the center bin of the peak. A normal hit message has a duration time of 2000 ns, thus multi hits can only take place in this time window.
Thus, the quantized pattern has its origin in the revolution of the electron bunch in the accelerator. The given quantization of 977 ns corresponds to the given revolution time of the DESY II accelerator accelerator (976 ns [D^+18]).
Due to the fact that large time differences have a decreasing appearance probability, the envelope shape decreases too. A plot with the same conditions as in Figure 7.4 but for a larger time window is shown in Figure 7.5.

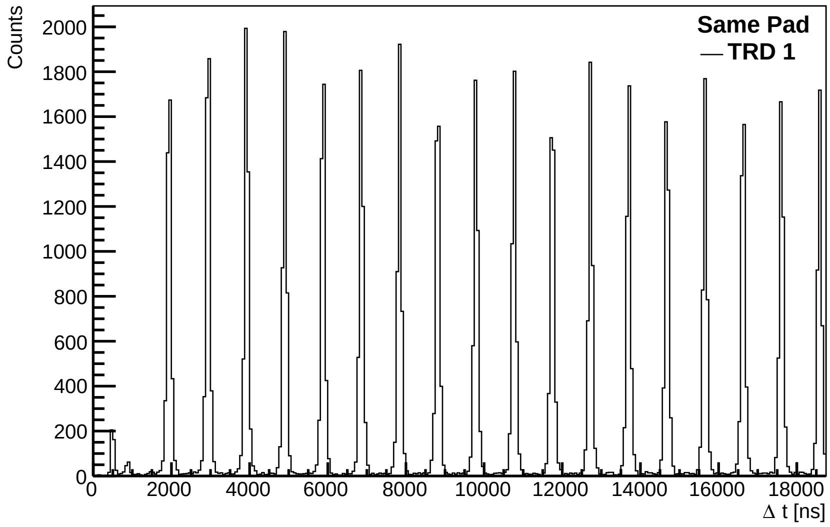

Figure 7.4: The time difference between two hits on the same pad is shown. In the short time region of 2000 ns multi hits may occur. The periodic pattern has its origin in the revolution of the electron bunch at the DESY II accelerator. The different peaks have a periodicity of ≈ 977 ns.

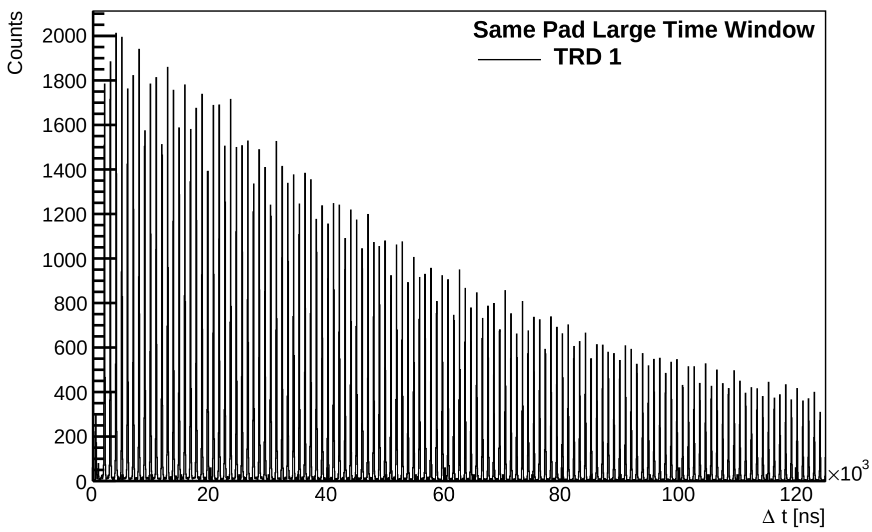

Figure 7.5: This plot fulfills the same conditions as the plot in Figure 7.4, but shows a longer timescale to visualize the decreasing height of the peaks.

7.2 Tail Retrigger

The analysis of the shapes shows that the data contains signals which differ from the expected shape. These can be identified as the tail of the original curve and is shown in Figure 7.6. The shapes in

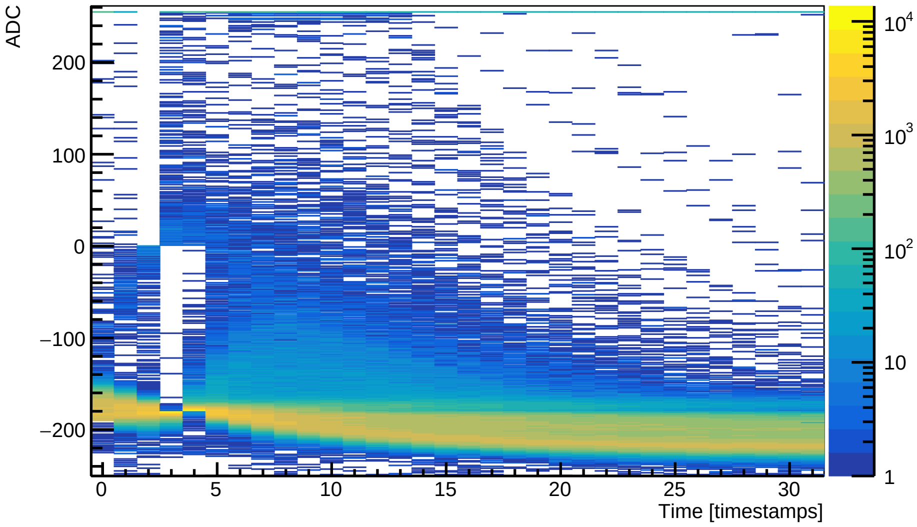

Figure 7.6: The tail retriggered shapes are shown. The long tails of the shaping functions are recognizable. Single normal signals are also captured. Those may be real multi hits. Some signals which are nearly continuously clipping do not the tail retrigger condition.

the figure have been extracted from a normal shape distribution by taking the signals in which the first ADC sample has a value larger than −190 ADU or the first bin features a higher value than the fifth bin. Signals from all layers were taken into account. A few real signals also fulfill the condition, but are neglected.

A possible explanation for this phenomenon could be noise large enough to overcome the trigger condition sitting on top of the expected tail of a normal signal falling below the trigger. Such a signal could be falsely identified as a multi hit.

7.3 Length of Hit Messages

In the following, the length of the hit messages is investigated. The examined shapes have to fulfill the conditions described in Chapter 7.1. Messages from all four layers were taken into account. The number of hit messages with the intended length of 32 time stamps is 916574, whereas the total number of hit messages with a shorter length is 386212. Thus, roughly 70.35 % of the hit messages are not interrupted by noise.

The hit message length distribution is shown in Figure 7.7. In order to make the peaks in this plot visible, messages with a length of 32 are omitted. Hit message lengths below a length of 5 timestamps are very rare due to the fact that the assembling algorithm developed by J. Beckhoff combines signals with a length of up to 5 clock cycles with its successor if directly following [Bec18]. Entries in this region may occur when the successor is not available due to some data transfer problems of the SPADIC. In this data set, none occur. The peaks with a length of 30 or 31 timestamps and around 16 time stamps may have their origin in the discussed quantization of the beam structure. The peak at the time stamp 23 is interpreted as the aforementioned tail retrigger, see Section 7.2. The first peak, representing messages with a length between 6 timestamps and 10 timestamps, shows that still additional retrigger effects occur. This may be induced by signal itself. The peak seems to be cut at the lower end, this may be an effect of the assembling algorithm.

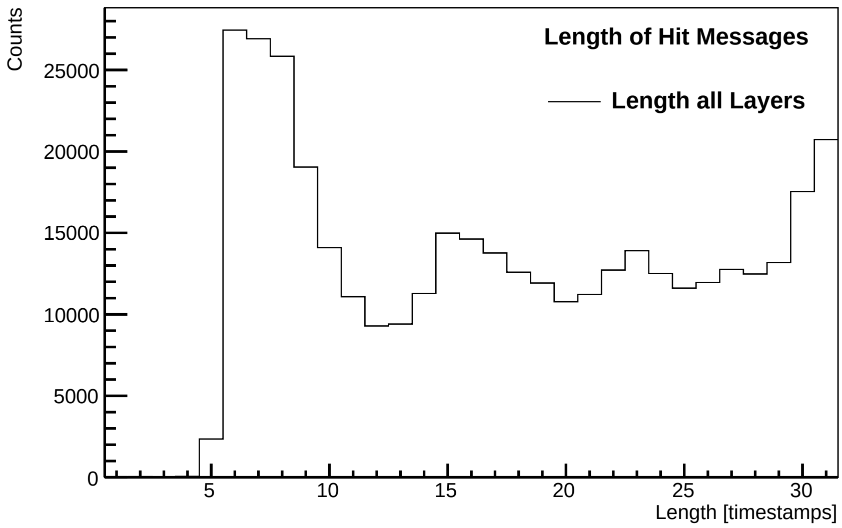

Figure 7.7: The length of the hit messages of all detector layers are shown. Hits of a length below 5 do not occur due to the assembling algorithm. The Peaks at 16 timestamps and 31 timestamps may be real multi hit events. The peak at 24 timestamps may be induced by the flank retrigger.

7.4 Beam Spot

To determine the illuminated area on the detectors, the hit messages on the pads were plotted into a histogram. Only hits of the trigger type 1 (*self triggered*) and 3 (*self and neighbor triggered*) were included. The illuminated area of the TRD at layer 1 is shown in Figure 7.8, the position is given relative to the border of the detector and is horizontal to the ground. The illuminated areas of layer 0 and layer 2 are given in the Appendix 10.2.

To give a dimension of the beam width, a Gaussian function is fitted to the histogram. This Gaussian does not fit the peak well ($\chi^2 = 12669$). The Gaussian fit to the distribution has its center at 55.3 cm and a σ of 0.8 cm. σ is the standard deviation. Due to the fact that the bin at 52.5 cm shows less entries than the bin at 52 cm, the illuminated area can be estimated between 52.5 cm and 57.5 cm. The right hand side of the illuminated area may be larger, but the pads at this area were not equipped with an additional SPADIC.

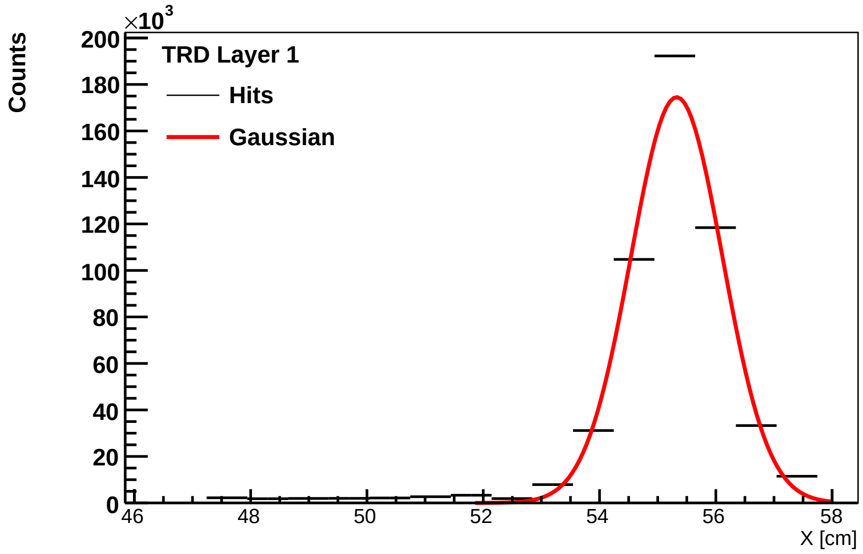

Figure 7.8: The hit message map of layer 1 is shown. For this investigation, only hit messages of the trigger type 1 and 3 were taken into account. The main signal stays between a horizontal position of 52.5 cm and 57.5 cm. The Gaussian does not reach the maximum of the distribution, but describes the bins at the outer region of the beam spot sufficiently.

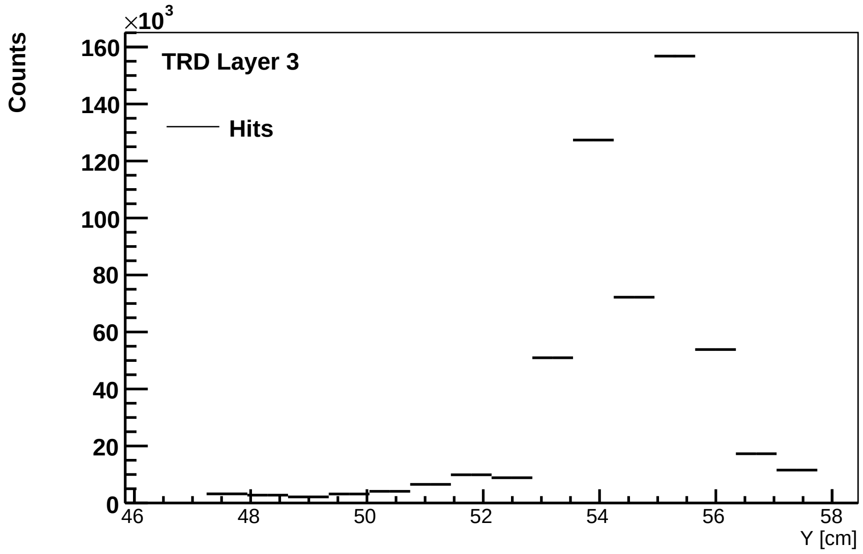

Figure 7.9: The hit map of layer 3 is shown. Only hits with the trigger type 1 and 3 were considered. The hit distribution does not conform to the expected shape. A real shape is not recognizable, most entries are in the expected beam spot region between 52.5 cm and 57.5 cm.

Since the detector is only able to obtain a position resolution in one direction, the last layer, layer 3, is rotated by 90 ° to measure the beam width in the other direction. Unfortunately, the data of layer 3 suffer unusual amounts of data losses and many signals have nothing in common with the designed and expected pulse shape. One example of a distorted shape is shown in the Appendix 10.1. The hit message distribution is shown in Figure 7.9; the bin at 54.7 cm has less entries than expected. The main part of the electron beam seems to stay between 52.5 cm and 57.5 cm in line with the expected dimension. A fit with a Gaussian function was not conducted. At the region between 49 cm and 52 cm the number of entries increases for positions closer to the expected beam spot.
The hole in the distribution may have its origins in the losses due to data leakage, this version of the front-end electronic is known for. This could be checked in detail by searching and assigning of info messages about the corresponding chip buffer status. Since the loss situation strongly depends on the exact position within the ASIC and its momentaneous load situation.

7.5 Cluster Analysis

Since the information of one hit in the detector is stored in different hit messages, those have to be aggregated to a group, which is called *cluster*. A cluster of hit messages is translated to a *hit* at the corresponding detector layer. The clusterisation has been conducted using the algorithm as described in [Mun16]. Particular measures have to be taken in order to stabilize the reconstruction against the retrigger (segmentation) phenomena seen with the ASIC version of this measurement.

7.5.1 Unexpected Cluster

To ensure the quality of the clusters, a cluster classification has been defined previously by P. Munkes. A cluster has to fulfill the following conditions to gets flagged as *normal*:

1 The number of hit messages must not be zero

2 The summarized charge must not be zero

3 Two hit messages with trigger type 2 (*neighbor triggered*) have to be contained

4 The number of hit messages has to be 3 or higher and a hit message with the trigger type 1 or 3 has to be contained.

If a cluster does not fulfilll all of these conditions, it gets flagged and the unfullfilled requirements gets noted. Condition 1 corresponds to *Empty*, 2 to *InvalidCharge*, 3 to *MissingFNR* and 4 to *MissingSTR*. Such a cluster is called *broken* cluster.
The analysis of the relation between *broken* and *normal* clusters shows that most of the clusters are not usable. A concrete disaggregation is given in Table 7.1. Only 24 % of the total number of clusters are flagged as *normal*. The percentage of broken clusters differs strongly in dependence of the layer. It is not known, why the only clusters with no charge are located in layer 1.
Since the main portion of the broken clusters has a missing *self* or *neighbor triggered* hit message, it is probable that the cluster algorithm misses some hit message and splits the cluster in two incomplete fragments.

Table 7.1: A concrete break down of the broken cluster condition is shown.

TRD layer	Normal	Broken	Empty	InvalideCharge	MissingFNR	MissingSTR
0	141283	1458907	0	27515	301698	1129694
1	569856	699031	266516	13314	202746	624177
2	185570	845224	0	15046	229290	603959
3	198847	1486911	0	28572	337097	1121242

In the analyzed data, 263812 hit messages have the trigger type 1 (*self triggered*), 671149 messages have the trigger type 2 (*neighbor triggered*), and 992747 hit messages have the trigger type 3 (*self and neighbor triggered*). These are a few to many hit messages with trigger type 2, but in general, the distribution is spread as expected. Thus, the hit messages for correct clusters are probably available.

7.5.2 Single Cluster Analysis

Since the number of reconstructed clusters is low, single clusters were analyzed to gain insight in the trigger patterns. An example for a complicated but not uncommon hit message is shown in Figure 7.10. This shows an example for a characteristic situation with the displaced retrigger effect which retriggers an already *neighbor* triggered pad as a *self* triggered pad. This effect mainly occurs in the timestamps behind the first trigger. Since the new self triggered signal has a full trigger pattern it stops the original signal. An algorithm has been developed which assembles the stopped hit messages with the succeeding hit messages. For a detailed description of the retrigger effect and the assembling algorithm see [Bec18].

To clarify the origins of the pattern, the assembling algorithm is deactivated. At the given hit message pattern, a *self* triggered signal occurs at the pads 1, 5, and 12. Each of those signals has a displaced retrigger. Those retriggers takes place at the pads 2, 6, and 13. This also triggers the neighbors, which stop the original *self* triggered signals, and an additional *neighbor* triggered hit message shifted by 1 time stamp relative to the beginning of the original cluster. The pattern gets even more complex since one of the events takes place at the border of the instrumented area and misses one *neighbor* triggered hit message.

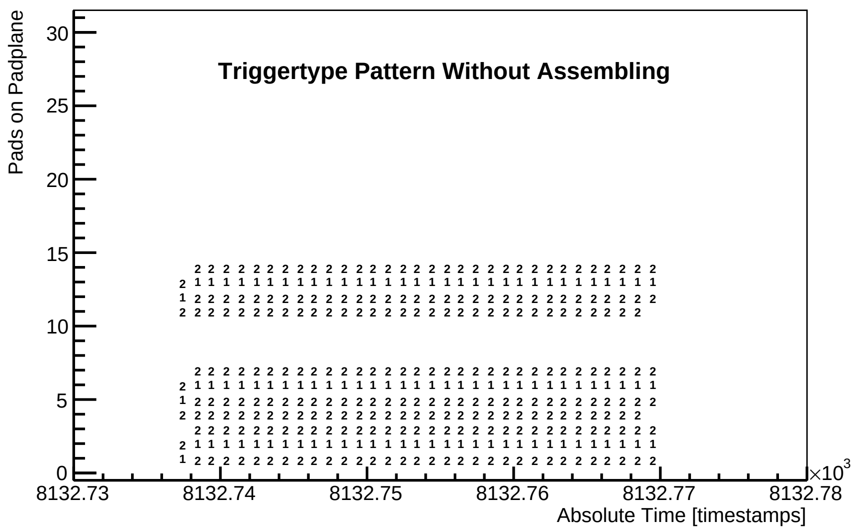

Figure 7.10: A complicated trigger pattern is shown; the assembling algorithm is deactivated. The pad numbers are plotted against the time given in time stamps. Each hit message is weighted by its trigger type to illustrate the pattern. Three signals are detected with the self triggered centers at the pads 1, 5, and 12. The cluster at the SPADIC border is not fully captured. Each signal has a displaced retrigger which stops the original signal.

If the assembling algorithm is used, this hit pattern changes. The first *self* and *neighbor* triggered pads are preserved, but the new triggered neighbor pads occur. The new pattern is shown in Figure 7.11.

It is very complicated to recognize the original hits in such a hit pattern and a very sophisticated cluster algorithm will be necessary to assign the hit messages to the right events. The actual algorithm is only able to recognize the hit with the 12th pad as center.

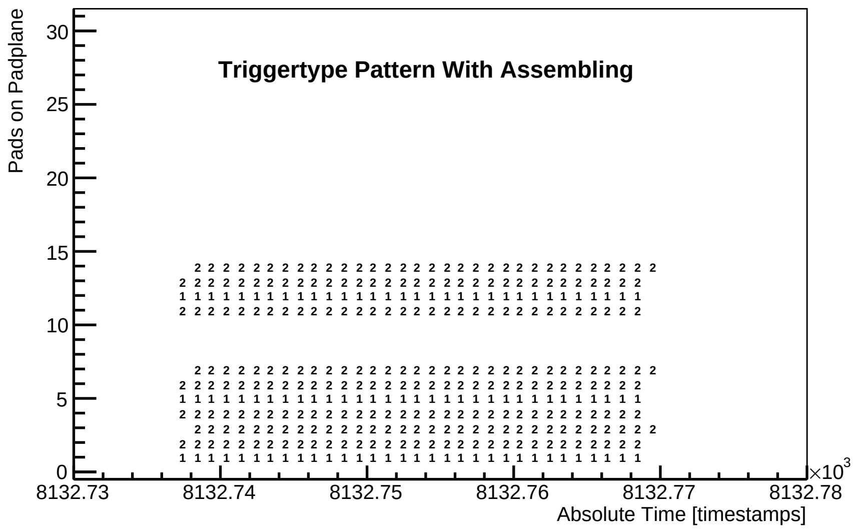

Figure 7.11: A complicated trigger pattern is shown, the assembling algorithm is activated. The pad numbers are plotted against the time in timestamps. The initial hits with the centers at the pads 1, 5, and 12 are assembled with the succeeding hit messages but the shifted FNR pads are preserved.

7.6 Further Cluster Analysis

Since the *broken* cluster has been examined, the build cluster has to be investigated. For this, the cluster size distribution is examined. The analysis of the distribution gives 943036 clusters which contain three hit messages, 4478 clusters with four hit messages, and 9286 clusters with five hit messages. The expectation is a higher amount of clusters containing four hit messages. Due to the fact that a high fraction of signals gets clipped by the ADC range, a non-negligible number of 4-pad clusters should occur.

The further analysis of the calculated displacements of the *normal* clusters shows problems with the position reconstruction. For 38733 clusters, the displacement is not even calculable. The cluster displacement distribution is shown in Figure 7.12. The calculated displacements are shifted by 1 pad width. A displacement of one corresponds to 1 pad width. That means, a perfect central hit has a displacement of 1 and a hit at the border a displacement of 0.5 pad widths or 1.5 pad widths. Those reconstructions have been done with the sech algorithm for 3-pad clusters and the cog algorithm for 4-pad clusters. Spikes in the distribution show that the displacements 0.5 pad widths, 1 pad width, and 1.5 pad widths are reconstructed to often. Since the main part of the calculated displacements is close to 1, the algorithm reconstructs more clusters at the pad center than at the pad borders.

The simulated position reconstruction shows that the reconstruction algorithms should reconstruct very precise displacements around 1.5 pad widths and 0.5 pad widths for a 3-pad cluster, see Figure 5.12 (in the simulated system, a simulated displacement of $\approx 3.5\,\mathrm{mm}$ corresponds to a measured displacement of 0.5 pad widths or 1.5 pad widths here) as for a 4-pad cluster, see Figure 5.15. So, the shift in the reconstruction algorithm is not the reason for the lower amount of clusters with a displacement close to 1.5 pad widths or 0.5 pad widths. Due to the fact that the illuminated area is larger than one pad width, shown in Section 7.4, the hits should not only be distributed close to the pad centers. It seems that the lack of 4-pad clusters is the reason, since 4-pad cluster are expected to have a displacement close to 1.5 pad widths or 0.5 pad widths.
A beam profile reconstructed with the clusters is given in Figure 7.13. The dips in the distribution may be another artifact by the missing 4-pad clusters or the not exact reconstructed displacements. The distance between the dips of 7.3 mm, the pad width, confirms that. The spikes, visible at the main peak and the left peak, may be a consequence of the artifacts seen in Figure 7.12. The main part of the entries has an x position between 53 cm and 57 cm. This fits roughly with the distribution of the self triggered hit messages in Chapter 7.4. The gaussian fit is obviously influenced by the dips of the distribution ($\chi^2 = 25628.3$). The width of this fit yields a beam width of $\sigma = 0.7\,\mathrm{cm}$.
Since a plausible reconstruction of the displacements is part of the latest developments, further investigations have to be done.

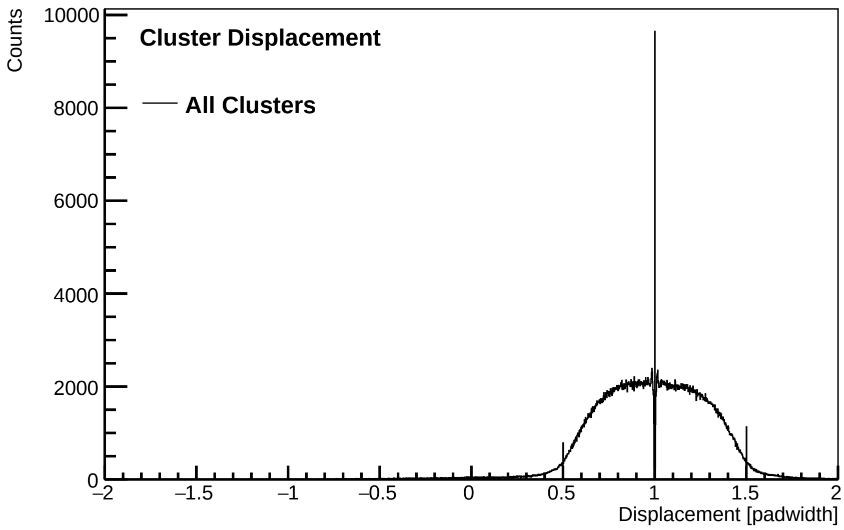

Figure 7.12: The calculated cluster displacements are shown. The whole distribution is shifted by 1 pad width and the main part of the clusters have a displacement close to 1. Displacements of 0.5 pad widths, 1 pad width, and 1.5 pad widths are calculated significantly more often. That seems to be an artifact.

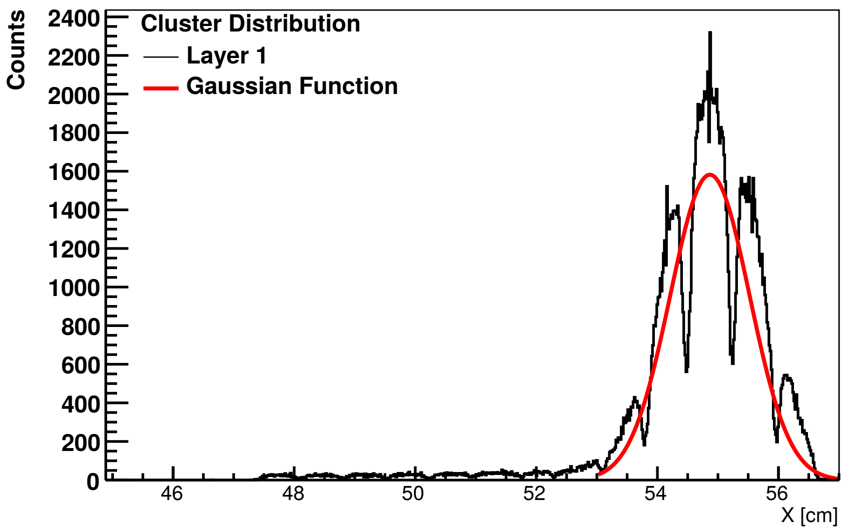

Figure 7.13: The cluster distribution of layer 1 is shown. The dips in the distribution have a distance of 7.3 mm; the pad width. Spikes in the distributions are visible, those may correspondent to the artifacts of Figure 7.12. The main part of the events stay between an x position of 53 cm and 57 cm.

8 Steps Towards Tracking at DESY 2017 Testbeam Data

The next step after the development of algorithms for precise reconstruction of position and timing is the development of a tracking algorithm. On the other hand, the data basis turned out to suffer from complex segmentation and data loss issues: 76 % of the built clusters can not build correctly and the remaining 24 % clusters partly have problems in the displacement reconstruction. Due to these efficiency and biasing questions in the recorded data, the tracking algorithm was not optimized further on real data. Regardless of the incompleteness, the idea of the first steps of this algorithm will be described.

The distance between the first and the last detector used in this analysis is 1.71 m as shown in Figure 6.4. With the approximation, that the speed of the electrons is equal to the speed of light, the time difference between the detection of the first hit on the first layer and the last hit on the last layer was 5.7 ns. Since one time bin in the presented system has a length of 62.5 ns, over 90 % of the tracks has been detected within the same electronic clock cycle (”timestamp”). All hits with the same time stamp are collected as a track candidate. If such a candidate cumulates two or less hits in it or the hits are distributed on two or less layers, it gets refused.

After that, a hit on the first layer gets picked. If there is no hit on the first layer, a hit of the second layer gets picked. Than, a hit on the following layer gets picked and the position difference of the projection of this hit on the first layer to the first hit is determined. If two hits on the second layer are available, the same procedure is done with the second hit. The hit with the smallest distance is picked. If the position difference between the closest hit is bigger than 3 times the measured beam width, the track candidate gets refused. In this implementation, the beam width is defined as σ of a Gaussian fit to the hit distribution of each layer. If there is no hit on the following layer, the same procedure starts at the subsequent layer.

To find a third hit, the procedure is the same as in the iteration before, but this time, the position difference of the new hit is calculated in relation to the intersection point of the prolongation of the line between the first and the second hit with the examined layer. The last step is repeated for a possible fourth hit on the last layer.

Since the position of the detectors were changed between some runs, an algorithm orientates the position of the chambers at the center of the beam spot.

Figure 8.1 shows a possible track candidate. Five hit messages were detected with the same time stamp. The z axis marks the acceptance status of the hit: 2 for hits of the track candidate, 1 for rejected hits. The rejected hit at the first layer seems to be closer to the prolongation of the straight line between the track hits on the second and third layer. Different track candidates should be compared and the track should be chosen by the probability of the track candidates. This example

shows that the algorithm is able to find first track candidates, but more development work has to be done.
Since the average event rate in the given data is small, two isochronous tracks should be uncommon and explicit assigning of the hits to a track should be feasible.
The analysis of tracks gives the possibility to investigate e.g. the scattering behavior, analysis of track angles, test of the position resolution.

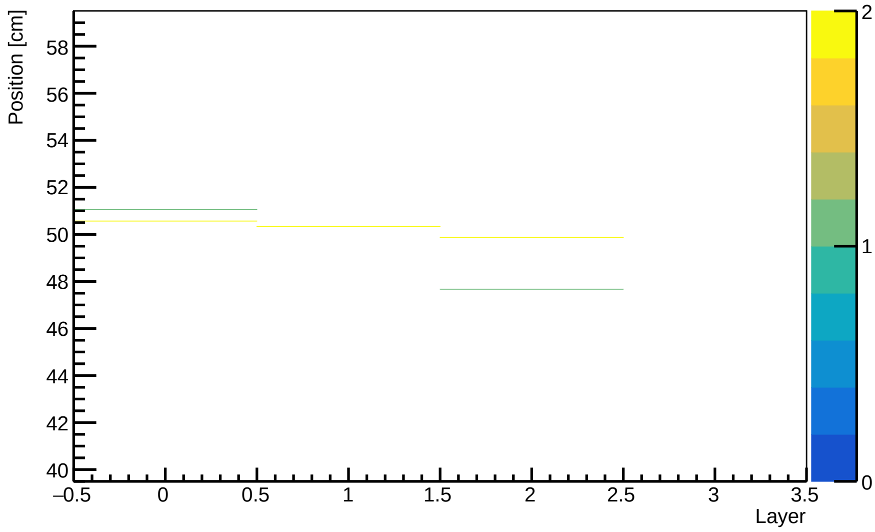

Figure 8.1: A track candidate is shown. The X position of the hits is plotted against the detector layers. The z value 2 is for a hit of the track candidate, the value 1 for a rejected hit. The rejected hit at the first layer may be a better hit candidate for the track.

9 Conclusion and Outlook

In several steps, a gas system for the mCBM testbeam campaign has been developed. A prototype of the system has been tested at the SPS 2016 testbeam campaign, at the DESY 2017 testbeam campaign, at the GIF^{++} 2017 testbeam campaign and during measurements in the laboratories in Münster. Several improvements have been done for the measurements at mCBM. The final system has been installed at the mCBM cave in 2019 and provides the installed TRD prototypes with the desired gas mixture, see Chapter 4.

In a simulation program, designed and build from scratch, code for the test and development of a precise time reconstruction for real data has been developed, see Section 5.1. These simulations may be the basis for improved precision in the time reconstruction of charge depositions in the detector. For further investigations the simulated pulses should be fully tuned according to the pulses in real data (e.g. noise level, ion tail). Shift effects due to the trigger threshold in dependence on the energy distribution of the incoming particles have to be examined. The analysis and comparison to real data are currently being prepared.

A second code set has been programmed to test the implemented position reconstruction algorithms, see Section 5.2. In the case of the 3-pad cluster simulations, the sech algorithm and the cog algorithm were tested, and altogether the sech algorithm shows the better performance. Both algorithms shift the position of the reconstructed hits. The relation between the calculated and simulated positions have been determined to correct those shifts, see Section 5.2.1.

Tests of hits with 4 triggering pads show that the implemented position reconstruction algorithm, a combination of the sech algorithm and an average, is not useful. Also, other reconstruction algorithms have been tested and were rejected. Among the tested algorithms, the favored method for position reconstruction of 4-pad clusters is the 4-pad cog algorithm. This algorithm also has a shift to the simulated position. The size of this shift has been determined. A position correction was implemented to account for it in the data, see Section 5.2.2.

The results of those simulations may help to reduce the characteristic distortions of the chosen reconstruction algorithm on the precision of the position reconstruction. This must be checked with real data, to verify the practical usability.

Data from the DESY testbeam campaign have been analyzed with focus on different topics. Typical time characteristics of the DESY beam line have been found, thereby checks of the timing of the data acquisition were possible. The revolution time of the DESY II accelerator has been found in the measurements of the time differences between two hits which hit the same pad. The determined revolution time of 977 ns is close to the revolution time of 976 ns determined by the DESY testbeam crew, see Section 7.1 [D^{+}18]. During this measurement, a filter to reduce the noise has been developed. This filter identifies roughly 27 % of the hits as non-physical triggers.

Characteristic behavior of the trigger mechanism has been worked out, which enables to stabilize future operations for more efficient data reconstruction, see Section 7.2.
The illuminated area of the detectors has been determined with the analysis of single hit messages. The detector at layer 3 had major data losses in most of the runs. The losses happen irregularly in the recorded data and cut originate from a specific data loss problem in the readout electronics or connection issues at this particular detector, see Section 7.4. At future testbeam campaigns, the online analysis should intensify the checks on the incoming data, e.g. concerning the detected shapes and the hit distribution on each layer.
The analysis of the clusters shows that only 24 % of the clusters get flagged to be reconstructed correctly. Due to the fact that the main part of the unexpected clusters misses some hit messages but the distribution of trigger types is nearly as expected, the cluster algorithm appears yet to not work with the expected efficiency, see Section 7.5.1. The analysis of the cluster width distribution shows that the 4-pad clusters are vastly underrepresented. This may be the reason for the dips in the position distribution of the clusters, but the found artifacts in the cluster displacement distribution have to be checked either, see Section 7.6. The analysis of single events displays that the hit message pattern can be much more complicated than expected, see Section 7.5.2. An improved, stable cluster finding algorithm will be necessary to continue with the analysis of the data from the DESY 2017 testbeam campaign. Also enabled by the results of this research, first steps of a further data analysis could be started [PK19].
Furthermore, an early tracking algorithm has been programmed in the course of this master project, see Chapter 8.
The key to further examinations of the data of the DESY 2017 testbeam campaign will be a cluster building algorithm which is stabilized against the found fragmentation of signals. Anyhow, detailed checks of possible biasing caused by unavoidable data selection turned out to be necessary. Due to the fact that the SPADIC 2.0 has been reworked since the testbeam campaign and with the given trigger particularities, such a cluster algorithm would be specific for the DESY 2017 testbeam campaign. Examinations of data measured with a setup closer to the final system may be a faster way to get improvements in the precise position and timing reconstruction.

10 Appendix

10.1 Shapes of Layer 3

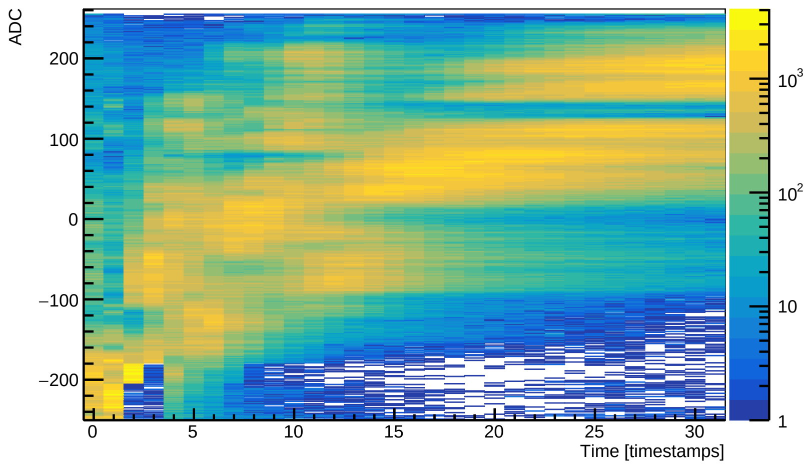

Figure 10.1: The shapes of layer 3 of run 112 are shown. They have nothing in common with the normal shape of the shaper.

10.2 Illuminated Areas

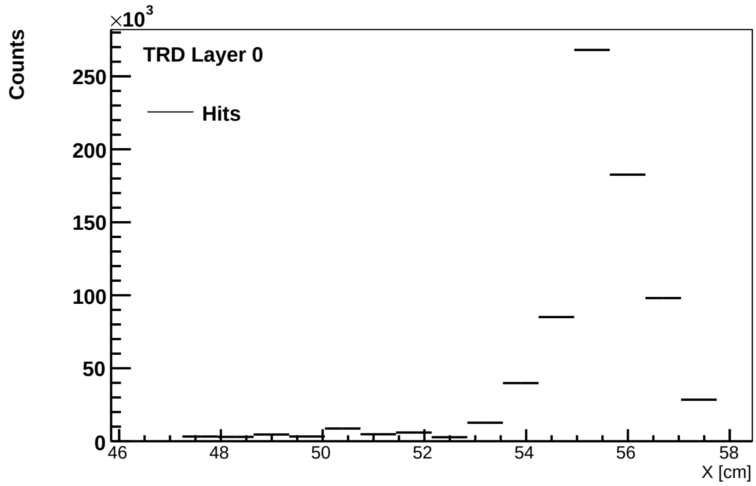

Figure 10.2: The illuminated area of layer 0 is shown. The main part of the hit messages takes place between 53 cm and 58 cm. The shown hit messages have the trigger type 1 (*self triggered*) and 3 (*self and neighbor triggered*). The data was taken from run 111.

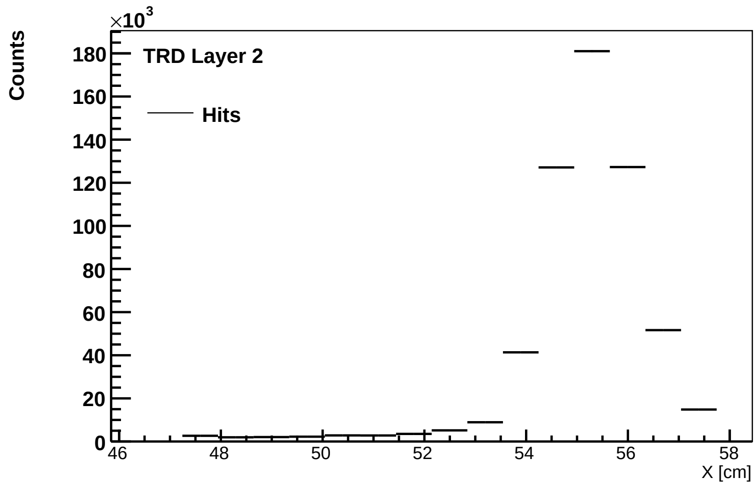

Figure 10.3: The illuminated area of layer 0 is shown. The main part of the hit messages takes place between 52 cm and 58 cm. The shown hit messages have the trigger type 1 and 3. The data was taken from run 111.

Bibliography

[And20] A. Andronic. Private communication. 2020.

[AW12] A. Andronic and J. P. Wessels. Transition radiation detectors. *Nuclear Instruments and Methods in Physics Research A*, 666:130–147, February 2012.

[Bec18] J. Beckhoff. Automated Test Stand Setup and Signal Reconstruction for the CBM-TRD, Master Thesis, 2018.

[Ber14] C. Bergmann. Development, Simulation and Test of Transition Radiation Detector Prototypes for the Compressed Baryonic Matter Experiment at the Facility for Antiproton and Ion Research, 2014.

[BR] R. Brun and F. Rademakers. Root - an object oriented data analysis framework. *Proceedings AIHENP'96 Workshop.*

[BRR08] Walter Blum, Luigi Rolandi, and Werner Riegler. *Particle detection with drift chambers.* Particle Acceleration and Detection. 2008.

[D$^+$18] R. Diener et al. The DESY II Test Beam Facility. 2018.

[des17] https://particle-physics.desy.de/e252106/e252106/e252211, Accessed: 10.08.2020, 2017.

[Fis] P. Fischer. *SPADIC2.2 Chip Manual, Version 1.1.*

[Hac] Hach. *ORBISPHERE Model K-M1100 Sensor and Model 410 Analyzer.*

[K$^+$17] M. Kohn et al. Analysis of the SPADIC multi-hit feature. *CBM Progress Report*, 2017.

[Kle05] K. Kleinknecht. *Detektoren für Teichenstrahlung, 4. Auflage.* 2005.

[Kob18] Kobold. *Kleinstmengen-Duchflussmesser/-wächter*, 2018.

[Kri14] M. Krieger. *SPADIC 1.0 Data Sheet*, 2014.

[MA16] A. Meyer-Ahrens. Auslese eines Szintillationszählers mit selbstgetriggerter Elektronik, Bachelor Thesis, 2016.

[MA19] A. Meyer-Ahrens. Electron Detection Efficiency of the CBM-TRD Prototypes in Testbeams at DESY, Master Thesis, 2019.

[Mat88] E. Mathieson. Cathode charge distributions in multiwire chambers: 4. empirical formula for small anode-cathode separation. *Nuclear Instruments and Methods in Physics Research*, 1988.

[Mun16] P. Munkes. Ereignis-Rekonstruktion für CBM TRD-Testdaten, Bachelor Thesis, 2016.

[pad20] http://cbm.uni-muenster.de/padplane/, Accessed: 10.08.2020, 2020.

[PK19] A. Puntke P. Kähler. Position reconstruction in DESY 2017 testbeam data. *CBM Progressreport*, 2019.

[T$^+$18] M. Tanabashi et al. Review of Particle Physics. *Phys. Rev.*, D98(3):030001, 2018.

[tdr18] The Transition Radiation Detector of the CBM Experiment at FAIR : Technical Design Report for the CBM Transition Radiation Detector (TRD). Technical Report FAIR Technical Design Report, Darmstadt, 2018.

[voe12] *Voegtling Manual: Mass flow meter and controller, pressure controller red-y smart series*, 2012.

Danksagungen

Insbesondere möchte ich Prof. Dr. Christian Klein-Bösing und Prof. Dr. Anton Andronic für das Ermöglichen dieser Arbeit und der Unterstützung vor allem bei komplexeren Fragestellungen danken. Darüber hinaus möchte ich Philipp Kähler für seine guten Ratschläge und seine Hilfsbereitschaft danken. Des Weiteren geht mein Dank an die restliche "CBM Münster-Crew" für eine tolle Atmosphäre und die uneingeschränkte Kollegialität. Der ganzen Arbeitsgruppe möchte ich danken für anregende Gespräche und Diskussionen auch über die Themen der Physik hinaus.

Plagiatserklärung

Hiermit versichere ich, dass die vorliegende Arbeit *Construction of a Gas System for the CBM-TRD Prototypes and Analysis of CBM-TRD Test Beam Data Towards Position Reconstruction* selbstständig verfasst worden ist, dass keine anderen Quellen und Hilfsmittel als die angegebenen benutzt worden sind und dass die Stellen der Arbeit, die anderen Werken – auch elektronischen Medien – dem Wortlaut oder Sinn nach entnommen wurden, auf jeden Fall unter Angabe der Quelle als Entlehnung kenntlich gemacht worden sind.

Ich erkläre mich mit einem Abgleich der Arbeit mit anderen Texten zwecks Auffindung von Übereinstimmungen sowie mit einer zu diesem Zweck vorzunehmenden Speicherung der Arbeit in eine Datenbank einverstanden.